Copper doped ceria catalyst prepared by reverse microemulsion method for thermocatalytic conversion of carbon dioxide via reverse water gas shift

by

Kishore Subramanian Kandasamy

A thesis

presented to the University of Waterloo

in fulfillment of the

thesis requirement for the degree of

Master of Applied Science

in

Chemical Engineering

Waterloo, Ontario, Canada, 2023

Author’s declaration

I hereby declare that I am the sole author of this thesis. This is a true copy of the thesis, including any required final revisions, as accepted by my examiners.

I understand that my thesis may be made electronically available to the public.

Abstract

In recent years, there has been a growing interest in catalytic reduction CO_2 as a response to the pressing environmental concern associated with it. Thermocatalytic reduction of CO_2 utilizing renewable H_2 has been promising as a potential solution to address these challenges. In this study, $CeO_2/\gamma\text{-}Al_2O_3$ and Cu/CeO_2 catalyst were studied for the reverse water gas shift reaction. An extensive investigation has been conducted towards reverse water gas shift reaction including reaction tests, and several characterization which includes, but not limited to, X-Ray diffraction, X-Ray spectroscopy and temperature programmed desorption

High surface area $CeO_2/\gamma\text{-}Al_2O_3$ nano-catalysts were synthesized via the reverse microemulsion method and evaluated for reverse water gas shift. The effect of the active phase dispersion on the CeO_2 nanoparticle growth was investigated via X-ray diffraction and gas adsorption. The 47.9wt% CeO_2/Al_2O_3 catalyst showed complete selectivity to CO generation while attaining nearly equilibrium values for CO_2 conversion at 600 °C and 8,000 mL/(g h). As compared to bulk CeO_2, nanoparticle growth in the CeO_2/Al_2O_3 catalyst was hindered significantly, resulting in a relatively stable catalytic performance, similar to that of the bulk CeO_2. Our findings reveal that the reverse microemulsion synthesized $\gamma\text{-}Al_2O_3$ support significantly decreases CeO_2 nanoparticle growth and agglomeration. This reduction in nanoparticle sintering contributes to the enhanced catalytic performance and stability, facilitating efficient CO_2 reduction.

Copper-doped ceria ($CuCeO_2$) catalysts with 0-26.5 Cu/(Cu+Ce) at% were synthesized via the reverse microemulsion method. X-ray diffraction analysis of freshly synthesized and

spent (post-reaction) catalysts showed no separate phase of copper of copper oxide, indicating that Cu was incorporated into the CeO_2 lattice, replacing Ce. Temperature programmed desorption experiments showed that the activation energy of CO_2 desorption increased for higher Cu loadings, indicating stronger CO_2 adsorption. This phenomenon was attributed to enhanced formation of oxygen vacancies due to Cu doping. X-ray photoelectron spectroscopy further confirmed the enhanced generation of oxygen vacancies due to Cu incorporation. Catalytic performance showed that all catalysts were 100% selective to CO generation, with higher Cu loadings resulting in CO_2 conversion close to equilibrium values. The activation energy of the reaction, determined through reaction tests, exhibited a linear relationship with the activation energy of CO_2 desorption. The relationship between these two energy barriers is explored, providing valuable insights into the catalytic mechanisms for RWGS.

Acknowledgements

I would like to thank my supervisor Professor David Simakov and Professor Aiping Yu for their continuous support and patient guidance during my program.

I would also like to thank my committee numbers: Professor Anna Klinkova, Professor Eric Croiset for their precious comments and suggestions on my project.

This work would not have been possible without the help and advice from my groupmates Yue Yu, Muhammad Waqas, Guanjie Sun, Yichen Zhuang, and Edris Madadian

I would also like to acknowledge the support of the Waterloo Institute of Sustainable Energy (WISE), the Ontario Centers of Excellence (OCE), the Canada Foundation for Innovation (CFI), and the Natural Science and Engineering Research Council (NSERC).

Finally, I would like to thank my parents and friends for their support and encouragement throughout my master's program.

Table of contents

List of figures

List of tables

Nomenclature

A	pre-exponential factor, mol/(s kg)
A_s	area occupied by a single surface atom, nm^2/CeO_2
D	dispersion of catalyst
d(SSA)	SSA-based particle size, nm
d(XRD)	XRD-based particle size, nm
E_a	activation energy, kJ/mol
$E_{a,des}$	activation energy of desorption, kJ/mol
$E_{a,rxn}$	activation energy of reaction, kJ/mol
F_i	input flow rate (i stands for either CO_2, CO, or CH_4), mol/s
f_1	CO_2 conversion to CO
f_2	CO_2 conversion to CH_4
ΔH°_{298}	reaction enthalpy, kJ/mol
K	Scherrer equation shape factor
M_W	molar mass of CeO_2, g/mol
N_a	Avogadro's number
P	pressure, bar
R_g	gas constant, $\mathrm{J/(K\ mol)}$
R	CO_2 conversion rate, mmol/(g s)
R_{max}	maximum CO_2 conversion rate, mmol/(g s)
R_{CO}	CO generation rate, mol/(s kg)
S_{CO}	CO selectivity
T	temperature, °C (K in Arrhenius equation)
T_{max}	peak temperature from TPD, °C
W_c	catalyst weight, kg
X_{CO_2}	CO_2 conversion
x	weight fraction, wt%
y_i	mole fraction (i stands for either CO_2, CO, or CH_4)

Greek letters

α	H_2:CO_2 ratio in the feed
B	full width at half maximum, radian

θ	diffraction angle, °
λ	X-ray wavelength, nm
ρ_i	material *i* density, g/cm^3
ρ_p	particle density, g/cm^3
ρ_p	bed density, g/cm^2
v_1	frequency factor, s^{-1}

Abbreviations

BET	Brunauer–Emmett–Teller
CB	carbon balance
CCS	carbon capture and storage
CCU	carbon capture and utilization
FTIR	Fourier transform infrared spectroscopy
GHSV	greenhouse gas
GHSV	gas hourly space velocity
ICP-OES	inductively coupled plasma optical emission spectroscopy
IR	infrared
RME	reverse microemulsion
RWGS	reverse water gas shift
SSA	specific surface area
TGA	thermo-gravimetric analysis
TOF	turnover frequency, s-1
TPD	temperature programmed desorption
TWC	three-way catalyst
WGS	water gas shift
XRD	X-ray diffraction
XPS	X-ray photoelectron spectroscopy

Chapter 1: Background

1.1 CO_2 and global emission

Climate change is an increasingly problematic phenomenon due to the severity of its impact on the entire world. Greenhouse gases (GHG) are the main contributors to this problem as they trap heat and raise the temperature of the planet. Among the greenhouse gases, CO_2 accounts for significant portion of the global greenhouse gas emission. The driving forces of the emissions consists of two categories: natural events (volcanic eruption, variation in solar radiation and earth's orbit) and anthropogenic events (power generation, agricultural livestock and industrial processes). Though natural and anthropogenic effects contribute to global warming, the influence of natural events is much smaller than that of human activities. According to the U.S. geological survey, the global CO_2 emissions from all volcanoes last year is estimated to be between 0.13 – 0.44Gt per year whereas global CO_2 emissions from energy combustion and industrial processes alone reached 36.3GT last year [1] . If CO_2 emissions continue to rise at the current rate, global temperature can exceed 1.5°C by 2040 which will lead to increased human death, water scarcity and ecosystem disruption [1]. As a result, identifying the main sources of problem and deriving solutions is very important to ensure the climate change problem can be tackled.

In the last 30 years, Canada's GHG emissions have increased by 13.9%, In 2021, the total GHG emissions emitted by Canada was 670 megatons of carbon dioxide equivalent (Mt CO_2, eq) which is a 1.8% increase from 2020 **(Figure 1)**.

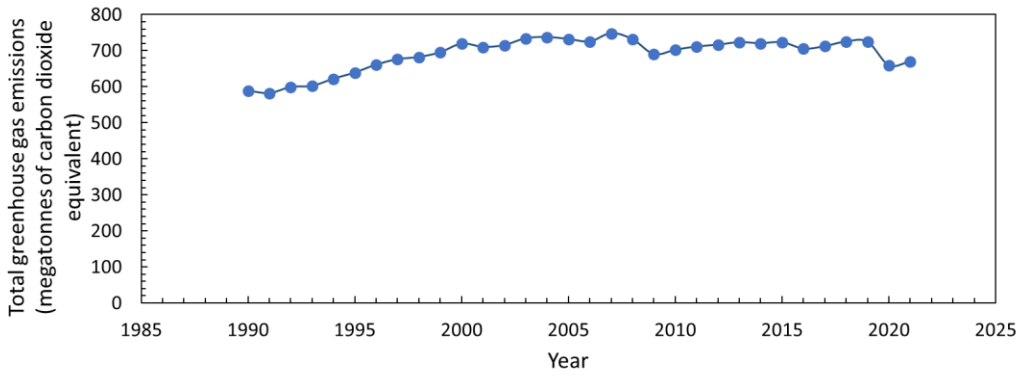

Figure 1. Greenhouse gases emission in Canada from 1990 to 2021 [2]

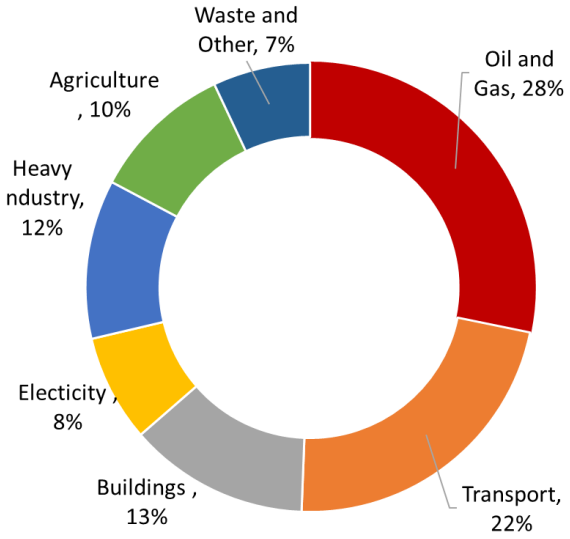

Figure 2. GHG emissions breakdown by economic sector in 2021 [3]

It is also important to understand where the GHG emissions are emitted from. In 2021, the environmental and climate change department of Canada determined that the main contributor to the GHG emissions was the oil and gas sector (with 189 Mt CO_2 emitted into the atmosphere), followed by the transportation industry (**Figure 2**). The GHG emissions

from the oil and gas sector rose by 3% compared to the previous year (2020). As seen in **Figure 3**, from 1990 to 2021, there was a rapid increase in the production of oil from oil sands. Oil sands production is more GHG-intensive than conventional sources leading to a significant impact on emissions from the oil and gas industry [2].

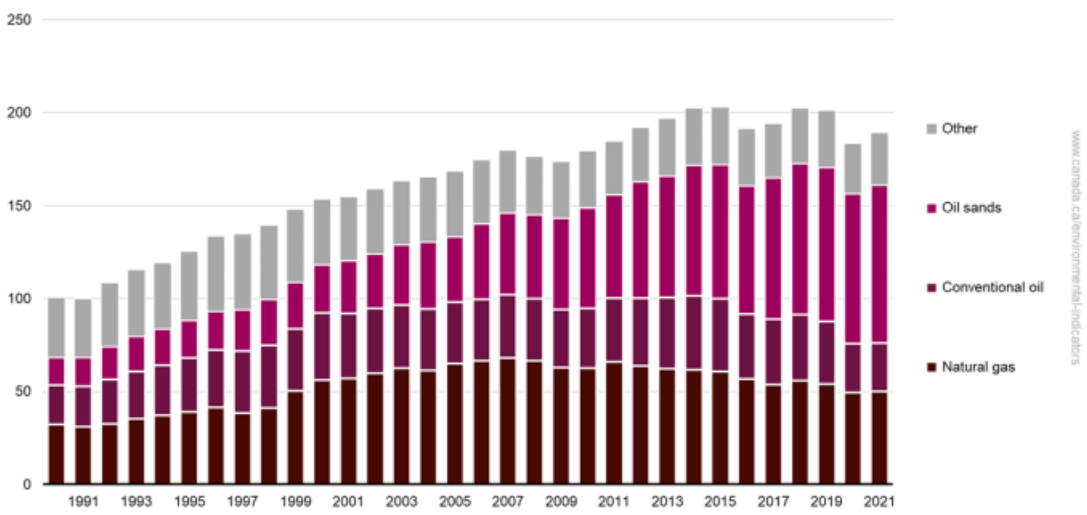

Figure 3. Oil and gas sector greenhouse gas emissions in Canada, 1990 to 2021

The data presented thus far highlights the urgent need for a viable solution to address this issue. A possible sustainable solution to tackle this problem is to close the carbon loop by converting CO_2 into valuable products, thereby reducing our dependence on fossil fuels. This transition towards sustainable alternatives will not only mitigate greenhouse gas emissions but also promote a more sustainable and environmentally friendly energy system.

1.2 Reaction pathways for CO_2

The scope of the problem has incentivized academia and industry to develop new technologies that focus on reducing CO_2 emissions, specifically, CO_2 capture and utilization has shown some promising application for CO_2 mitigation. Currently, the two

technologies with significant research are carbon capture and storage (CCS), and carbon capture and utilization (CCU). CCS is a promising solution for addressing the CO_2 problem as it separates CO_2 directly from the outlet stream and pumped underground. There are various processes being investigated for the separation of CO_2 from outlet streams, including amine scrubbing and membrane separation methods. However, the main obstacle for this technology to overcome is the large capital investment and lackluster economic returns [3]. Furthermore, the long term effects of storing carbon in underground reservoirs are unknown. Conversely, CCU has attracted a great amount of attention as CO_2 emissions can be converted to useful products such as synthetic fuel. The ability to create an artificial carbon loop and convert CO_2 emissions into profitable resources has accelerated research in this field.

There are many different reaction pathways that are explored for CO_2 utilization, which includes electrochemical, photochemical, biological and thermo-catalytic conversion [4]. Electrochemical and biological routes have attracted attention for reducing CO_2 to products such as methanol or formic acid. Electrochemical routes has shown some potential in achieving this goal, but it is limited by low CO_2 solubility in water and inherent diffusion limitation [5]. Biological routes also have major limitations, such as cost of cultivating large biological system [5]. Thermocatalytic conversion has become a more favorable option as it can combine high temperatures and catalytic reaction to provide high CO_2 conversion.

Thermocatalytic conversion relies on H_2 as a reactant for converting CO_2 into fuels and chemicals. Current methods of producing H_2 relies on commercial techniques like steam reforming of natural gas which generates GHGs. However, if H_2 can be produced through

electrolysis which is powered by renewable energy, the overall emissions for this process will reduce. In addition, if the CO_2 is taken directly from the emission source it will create an artificial carbon cycle thus making it more sustainable.

Figure 4 shows the reaction pathways to produce various chemicals. Methane can be reacted with water in the process of methane steam reforming (MSR) to produce syngas, a mixture of primarily CO and H_2. In addition to this, methane can also react with CO_2 via methane dry reforming (MDR) to produce syngas as well. Another possible way to produce syngas is through reverse water gas shift reaction (RWGS). This reaction is a catalytic reaction between CO_2 and H_2 to produce syngas. The Sabatier reaction (SR) is an exothermic catalytic reaction between CO_2 and H_2 can form synthetic natural gas.

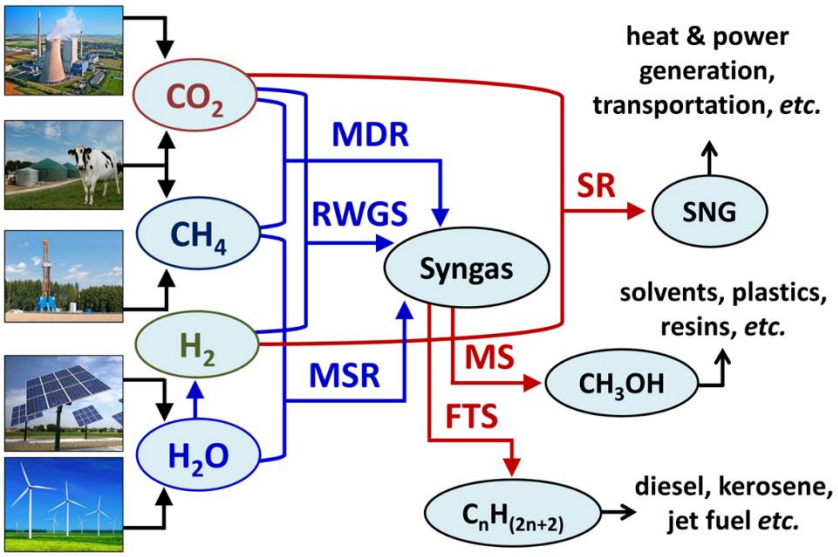

Figure 4. CO_2 reaction pathways for thermocatalytic hydrogenation [5]

Syngas is a valuable chemical as it serves as a precursor for a wide range of products, including fuels and solvents, among others. Syngas has many potential application such as converting to gasoline via Fischer-Tropsch process or to acetic acid via methanol synthesis.

The detailed pathways for syngas is shown in **Figure 5.** The project's focus on reverse water gas shift (RWGS) reaction is driven by the versatility of syngas and its potential to facilitate sustainable production of diverse valuable products. The capability to convert CO_2 into syngas opens up opportunities for environmentally-friendly synthesis of a wide range of valuable compounds.

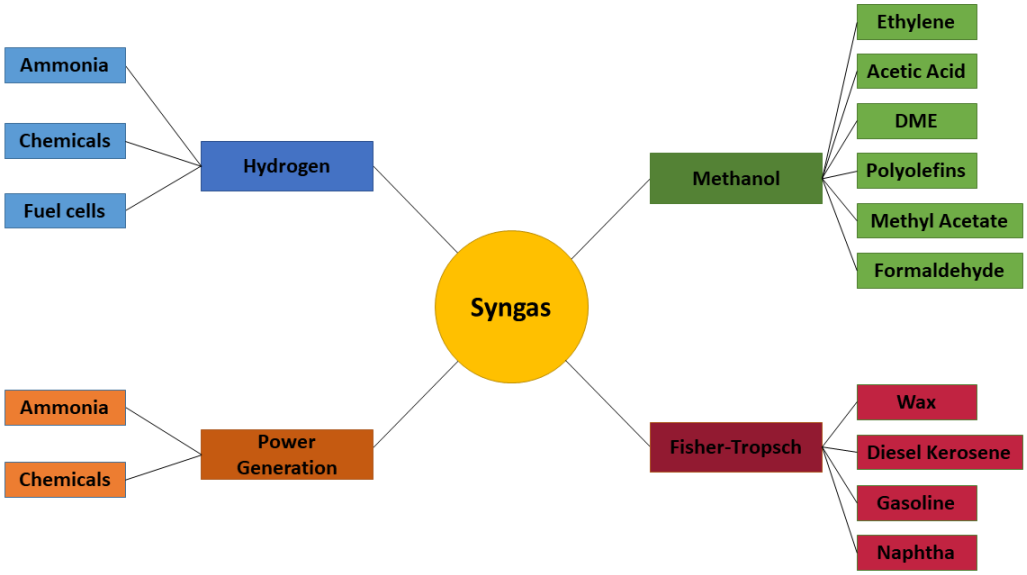

Figure 5. Syngas uses in different fields [6]

1.3 Reverse water gas shift

Reverse water gas shift (RWGS) is a key reaction for thermo-catalytic hydrogenation as the syngas mixture produced can be utilized as feedstock for various other reactions. RWGS is an endothermic process **(Eq. (1))** which is process which is typically accompanied with Sabatier reaction, **Eq. (2)**, and CO methanation **Eq. (3),** both leading to the formation of CH_4.

$$CO_2 + H_2 \rightleftarrows CO + H_2O \qquad \Delta H^{\circ}_{298} = +41.2 \text{ kJ/mol} \tag{1}$$

$$CO_2 + 4H_2 \rightleftarrows CH_4 + 2H_2O \qquad \Delta H^{\circ}_{298} = -164.9 \text{ kJ/mol} \tag{2}$$

$$CO + 3H_2 \rightleftarrows CH_4 + H_2O \qquad \Delta H^{\circ}_{298} = -206.5 \text{ kJ/mol} \tag{3}$$

In RWGS, CO_2 can be reduced to CO under excess H_2 in the feed product and appropriate catalyst and temperature. The advantage of using this reaction is that the option provides flexibility for the output product that can be produced [7].

Due to the endothermic nature of the RWGS reaction, high temperatures are required in order to achieve high conversion of CO_2 and high CO selectivity. However, conducting catalytic reactions at high temperatures may cause sintering or deactivation of the catalyst [8]. As a result, there is a strong need to develop catalysts that are highly active and selective to CO at lower temperatures (< 600°C).

1.4 Project objectives

Main goal:

The main goal of this thesis is to develop and evaluate CeO_2 based heterogeneous catalyst that is highly active towards the RWGS and selective to CO. Furthermore, comprehensive characterization process employing a diverse range of analytical techniques will be used to evaluate the catalyst. This extensive characterization aims to provide detailed insights into the structural, chemical, and physical properties of the catalysts that aid in promoting the activity for RWGS. The specific objectives for this project are:

1. Comprehensive study of nanoparticle growth and agglomeration of RME ceria in alumina-supported ceria catalyst under prolonged reaction condition
2. Evaluation of copper doped ceria catalyst synthesized via reverse microemulsion (RME) and evaluate the structure-activity relationship of the catalyst for the RWGS reaction

1.5 Thesis outline

Chapter 2 summarizes literature review for RWGS catalyst which includes, noble metal, transition metal and metal oxides catalyst.

Chapter 3 identifies the catalyst used for this project, along with the synthesis method used for this project. Chapter 3 also illustrates the characterization method used in this project to evaluate all the catalyst. This includes a brief schematic and explanation of characterization techniques like X-Ray diffraction, X-Ray spectroscopy and temperature programmed desorption. Additionally, a detailed schematic of the flow system utilized for the reaction test is also provided.

Chapter 4 deals with nanoparticle growth and agglomeration of RME ceria in alumina-supported ceria catalyst under prolonged reaction condition.

Chapter 5 presents the results of the copper doped ceria evaluated for RWGS. It includes both characterization and reaction test results for this project and some discussion on the structure activity relationship.

Finally chapter 6 briefly concludes the results presented and provides some insights on how this work can be improved.

Chapter 2: Literature review

2.1 Noble metal catalyst

Noble metal catalysts like Pt, Rh, and Ru have been extensively investigated for the RWGS reaction and have shown high activity [9]. The incomplete d-orbital combined with oxidation properties of noble metals resulted in excellent performance for RWGS reaction and promising corrosion resistant properties as well. Noble metal catalyst supported on Al_2O_3, CeO_2, and TiO_2 have shown to be very active for RWGS reaction. Pt-based catalysts can readily disperse on reducible metal oxides due to the abundant surface oxygen vacancies [10]. This facilitates the effective adsorption and activation of CO_2 [11]. Zhao et al. investigated two Pt/CeO_2 catalysts: atomically dispersed Pt species, and Pt clusters and particles with different sizes, to evaluate the effect of Pt dispersion on CO selectivity[9] . Reaction tests were conducted in a fixed bed reactor in the 200-450°C range, atmospheric pressure, at feed ratio of H_2:CO_2 = 4. Atomically dispersed Pt catalysts maintained a stable CO selectivity of 98% across the reaction temperatures, while the other samples experienced a significant decline, dropping from 98% to 32% within the temperature range of 400-450°C. CO-TPD results showed that Pt with larger sizes exhibited a strong adsorption to CO then the other samples which was crucial in preventing excess hydrogenation to CH_4. Kim et al. investigated Pt/TiO_2 catalyst for RWGS[12]. They showed that the metallic Pt in contact with Ti^{3+} has a high electron donating property due to the strong metal-support interaction. This leads to Pt-O_V- Ti^{3+} sites for CO production. CO_2 evaluated in quartz tube reaction in the temperature range of 300-600°C showed equilibrium conversion throughout all temperature further showing the importance of noble metal and support interaction for superior catalyst performance.

Ru based catalyst have also become attractive due to their incredible ability dissociate H_2. Ru were proved to be active for both CO_2 methanation and RWGS reaction and the selectivity for the respective reaction highly depends on the catalyst structure [13]. Tang et al. developed Ru based catalysts by encapsulating small clusters of Ru into hollow SiO_2 shells [14]. They found out that this catalyst configuration prevented sintering of the Ru clusters during the reaction. Their reaction test (T = 200-400°C, atmospheric pressure, at H_2:CO_2 = 1) conducted in quartz tube reactor showed the catalyst was 100% selective to CO at all temperature ranges. Furthermore, stability test conducted for 12h on stream (T = 400°C) had minimal loses in activity without changing CO selectivity.

Though noble metal catalyst show promising results for the RWGS reaction, the high cost associated with noble metals and the selectivity towards CH_4 limits the practical application of these catalyst.

2.2 Transition metal catalyst

Transition metal catalysts, such as Ni, Fe, and Cu, have garnered considerable attention due to their affordability and high activity in hydrogenation reactions such as the water gas shift reaction. Yang et. al. studied the effect of promoters like FeO_x and CeO_2 on Ni/Al_2O_3 catalyst synthesized by the wet impregnation method for RWGS reaction [15]. They showed CO_2 conversion close to equilibrium and excellent stability. The high conversion is attributed to the electronic enrichment of Ni atoms on the surface of the catalyst due to the FeO_x and Ni interaction. This electronic enrichment facilitated CO_2 adsorption which resulted in better performance. Though nickel catalyst showed good activity for CO_2 conversion, it is more selective to CH_4 at lower temperature which leads it to be more favorable for CH_4 then CO.

On the contrary, Fe based catalyst have shown significant activity towards RWGS and high CO selectivity. In the paper presented by Yang et al. [16] the iron copper oxide catalyst supported on CeO_2/Al_2O_3 with various Fe/Cu oxides ratio were investigated for the RWGS reaction. During the reaction, metallic Fe and Cu were formed which act as an active site for CO_2 activation. Reaction test (T = 440-750 °C, WHSV = 30,000 ml/(g h)) conducted in quartz tube reactor revealed conversion value close to equilibrium for Fe/Cu catalysts at high temperatures. The synergistic effect of Fe and Cu assisted the catalyst's excellent stability results. Fe-Mo bimetallic catalyst was investigated for RWGS by Kharaji et al [17]. Reaction tests conducted on a fixed bed flow reactor at $H_2/CO_2 = 1$ showed that CO yield was highest for $Fe\text{-}Mo/Al_2O_3$ followed by Fe/Al_2O_3, and Mo/Al_2O_3. The interaction of Fe-O-Mo in $Fe\text{-}Mo/Al_2O_3$ catalyst increases electron deficient state of Fe on the surface of catalyst which increases catalytic activity. Moreover the formation of $Fe_2(MoO_4)_3$ phase helped inhibit deactivation of the catalyst.

Cu based catalyst are widely investigated for RWGS due to its affordability and excellent activity towards RWGS reaction. Gao et al. investigated three different concentration of Cu/MoO_x (1:2, 1:1, 2:1) for the RWGS reaction [18]. The interaction of MoO_x support and Cu is responsible for a higher dispersion of Cu and produce more Cu-MoOx interface which leads to increased oxygen vacancies. XPS results confirmed that the ratio of surface oxygen to lattice oxygen was the lowest for 1:1 Cu/MoO_z. As a result, reaction test conducted in quartz fixed bed reactor (inlet flow rate 50.0 mL/min CO_2/H_2/Ar mixture gas (10/40/50)) resulted in a 35.85% CO_2 conversion and 99% selectivity for CO at 400 °C. Bahmanpour et al. studied the stability of Cu based catalyst by studying the spinel oxide Cu/Al catalyst. Stability test conducted at T = 600 °C, GHSV= 300 000 ml/(g

h), had conversion value of 47% (equilibrium conversion = 53%) and showed no deactivation in performance. Electron paramagnetic resonance results showed that the isolated Cu^{2+} ions strong interaction with Al_2O_3 may have potentially lead to the formation of a surface Cu–Al spinel. Furthermore, density functional theory (DFT) calculations indicated that the H_2 dissociation occurred on surface Cu ions while the stable surface adsorbates for both H_2 and CO_2 was formed on surface oxygen sites.

2.3 Ceria

Ceria (CeO_2) has been increasingly studied due to its wide usage as a support material and its strong reversible reducibility [19]. CeO_2 has high oxygen storage capacity and the ability to reversibly store and release oxygen, switching chemical states from Ce^{4+} to Ce^{3+} (through the formation of oxygen vacancies) [20]. Oxygen vacancies formed can be active sites for CO_2 adsorption, enhancing the catalytic activity for the RWGS reaction. CeO_2 has been well investigated for its usage as promoter or support, however, there are only a few studies that have investigated CeO_2 as an active phase for the RWGS reaction.

Dai et al. [21] investigated CeO_2 synthesized via hard-template, complex, and precipitation methods. Reaction tests were conducted in the 300-580 ºC range, at atmospheric pressure, feed ratio of H_2:CO_2 = 4, and GHSV = 60,000 mL/(g h). The obtained results showed that all catalysts were 100% selective to CO with the conversion ranging from 9-16% at 580 ºC (note that the equilibrium RWGS conversion is ca. 60% at this temperature). The hard-template-synthesized catalyst showed the highest conversion (16%) was achieved due to its porous structure and large specific surface area. Liu et al. [22] examined CeO_2 nanocube, nanorodes, and nanooctahedra that were synthesized by the hydrothermal method. Reaction tests showed CO_2 conversions of less than 10% for all

catalysts at 600 °C, 1 atm, and H_2:CO_2 = 1. Iqbal et al. [23]reported CeO_2 nanoparticles synthesized via the reverse microemulsion method (ca. 150 m^2/g, 4 nm nanoparticle size). Reaction tests showed significantly higher CO_2 conversions (45% at 600 °C, 3 bar, and H_2:CO_2 = 4), which is the highest CO_2 conversion reported for pure CeO_2 under similar reaction conditions.

2.4 Transition metal doped catalyst

Although CeO_2 was proven to be very selective to RWGS (no CH_4 formation), reported CO_2 conversions are mostly far from the equilibrium values. Generally speaking, CeO_2 is a relatively poor catalyst and is only capable of generating limited oxygen vacancies [24]. Many studies have shown that incorporating of transition metals into CeO_2 can significantly boost catalytic activity for the desired reaction pathway [25]. In particular, Ni, Cu, and Co can be easily integrated into the CeO_2 lattice to generate oxygen vacancies. CeO_2 can be also used as a support. E.g., Ru/CeO_2 was proved to be active for both CO_2 methanation and RWGS reactions, with the selectivity being highly depended on the Ru nanoparticle size [13]. Yttrium-modified Ni/CeO_2 catalysts were prepared by Sun et al. [26], demonstrating that CH_4 is the dominant product for Ni-based catalysts. It is interesting that Ni/CeO_2 is also a decent catalyst for methane dry reforming, and the catalytic performance can be further improved with Zr, Sm, and La dopants that can alter the interaction of Ni with the doped CeO_2 support [27]. Dai et al. [28] investigated the doping effect of several transition metals, including Ni, Co, Fe, Mn, and Cu, on the RWGS activity of mesoporous CeO_2. CeO_2 doped with Ni, Co, and Cu showed the highest conversion, while Cu, Fe, and Mn dopants provided 100% selectivity towards CO. In another study by Yang et al. [16], Fe-Cu/CeO_2-Al_2O_3 catalysts were prepared by wet impregnation and

tested for RWGS. The synthesized bimetallic catalysts showed superior conversion compared to monometallic catalysts, and all samples containing Cu showed excellent CO selectivity. It should be emphasized at this point that Cu-based catalysts were proven to be very active for RWGS [29].

2.5 Copper doped catalyst

Several studies have demonstrated that Cu can be incorporated into the CeO_2 lattice, changing its characteristics significantly [30], but only a few studies were reported for RWGS. Zhou et al. [24] investigated mesoporous Cu-doped CeO_2 with various Cu/Ce molar ratios synthesized by the hard template method for RWGS activity. The characterization results showed the formation of oxygen vacancies and Cu^0 species, which are the active sites. The CO_2 adsorption capacity of the catalyst was also enhanced. Liu et al. [31] studied RWGS over highly dispersed Cu clusters on CeO_2 with high Cu loading (15wt%) synthesized via deposition precipitation. It was reported that additional oxygen vacancies were generated by Cu doping, promoting the CO_2 activation. Reaction tests conducted at $H_2/CO_2 = 4$, atmospheric pressure, and 300-600 °C showed 100% selectivity to CO and CO_2 conversion of 59% at 600 °C (nearly equilibrium value). Ebrahami et al. [32] examined Cu/CeO_2 catalysts synthesized via solution combustion synthesis method. The X-ray diffraction results showed that Cu ions can easily replace Ce ions in the CeO_2 lattice. Reaction tests showed CO_2 conversion of 70% at 600 °C, atmospheric pressure, $H_2/CO_2 = 4$, and GHSV = 15,000 ml/(g h), with 100% selectivity to CO.

2.6 Reverse microemulsion synthesis for catalyst preparation

A suitable heterogeneous catalyst requires a series of advantages to be active for RWGS. The synthesis method should yield a catalyst that is in the nano scale, and has high surface area. In general catalytic activity is enhanced when the surface area of the catalyst increases, as there is more available catalytic sites. Due to this, researchers aim to synthesize smaller particle size, as this increases the surface area which, theoretically, increases the activity of the catalyst. Many different innovative synthesis method have been developed and studied so that the catalyst can be produced within a desirable size. Among the various synthesis method reverse microemulsion (RME) has proven to synthesize catalyst that are nano-scale and have high surface area. [33]

Microemulsion is a system of water, oil and surfactant that is transparent and thermodynamically stable. At macroscopic scale, the RME system appears to be homogenous, but in the microscopic scale it appears heterogeneous. The concentration of water and oil can change the system completely. At high water concentration, the internal structure of microemulsion consists of small oil droplets in a continuous water phase. As the concentration of oil increases, the internal structure changes to a continuous oil phase with small water droplets inside it [33]. The size of the droplets vary from 10nm-100nm and they plays a role in determining the size of the catalyst produced. **Figure 6** shows a typical reverse microemulsion system. The polar head groups of the surfactant molecules are attracted to the water droplets, whereas the hydrocarbon tail group is attracted to the oil phase [34]. A co-surfactant is also added to the microemulsion system as it helps lower the interfacial tension and increases the stability of the system [35].

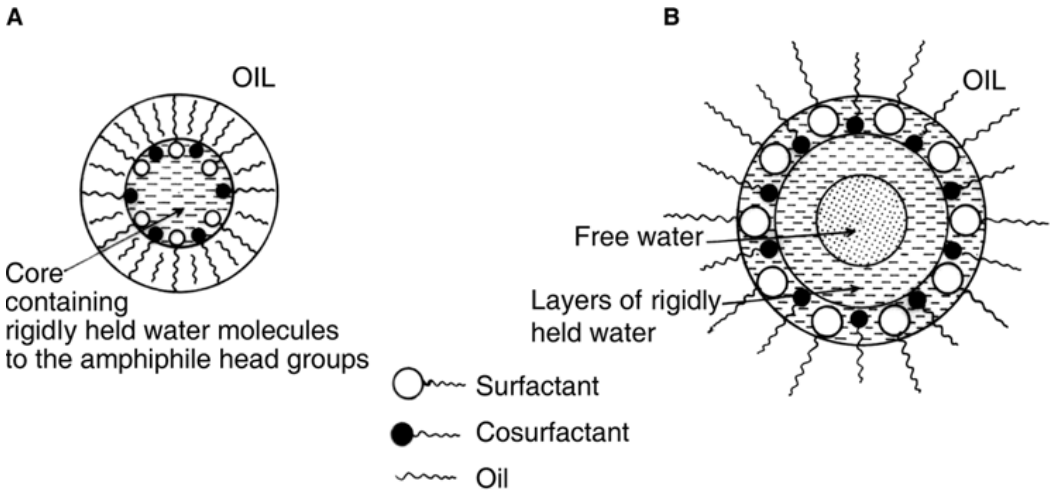

Figure 6. A sketch of RME nano-doplets[35].

RME is used as a synthesis method for nano-particle to ensure a narrow particle size distribution. The water droplets in RME systems have hydrophilic moiety that can help dissolve transition metal salts. This is particularly useful as these nano-doplets can be used as micro reactors to carry out chemical reactions. **Figure 7** illustrates the chemical route for nano-scale reaction with RME solutions. The salt precursor of the desired catalyst can be dissolved in one RME system, and a suitable reducing agent can be dissolved in another. When both the RME system are mixed together, intermicellar exchange of reactants allows for nano-scale reaction which produces the desired nano-particles. The RME reaction mechanism allows for particles to be generated that is very small and has a high surface area.

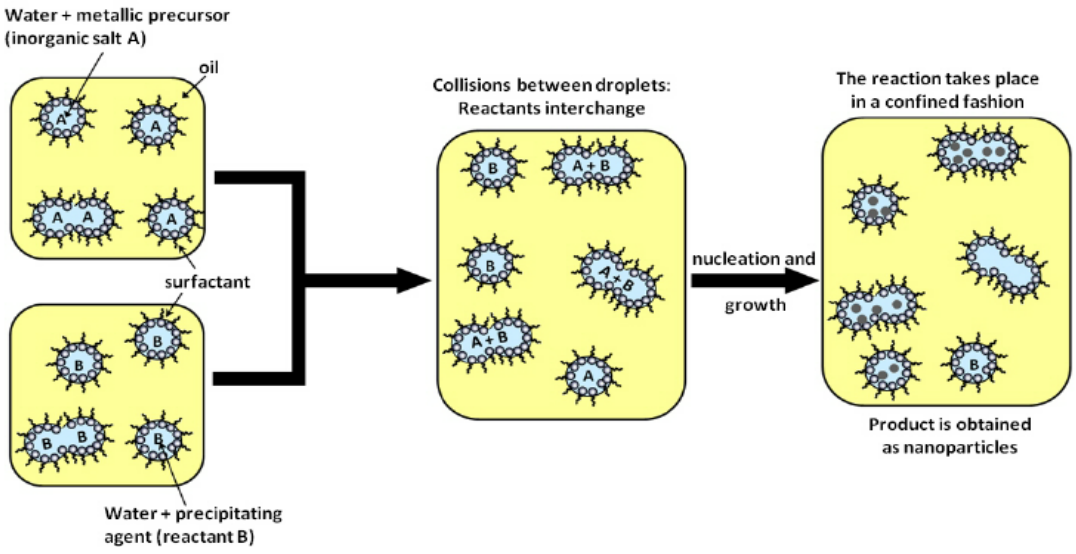

Figure 7. Schematic of two RME reaction method for the synthesis of nano-particles

In this project, RME synthesis method is employed to synthesize the catalysts. The composition of the RME solution consists of an aqueous phase, surfactant, co-surfactant and an oil phase. The ratio of these composition was selected from our group's previous work that was published last year [23]. The detailed synthesis method for the catalysts are reported in the next section.

Chapter 3: Methodology

3.1 Catalyst synthesis

Based on the literature review, CeO_2 shows promising results for RWGS due to its high oxygen storage capacity, chemical and thermal stability. In chapter 4, different weight concentration of $CeO_2/\gamma\text{-}Al_2O_3$ catalyst were evaluated for RWGS, specifically long term stability performance.

CeO_2 can also accommodate the substitution of Ce in its lattice by lanthanides, transition metals, and noble metals. This substitution can lead to the formation of defects and affect the migration ability of lattice oxygen within the CeO_2 structure. Cu has the ability to substitute Ce in CeO_2 lattice Therefore, in chapter 5, different concentrations of copper-doped ceria (x-$CuCeO_2$, where x denotes atomic percentage at %) were synthesized and evaluated for the RWGS reaction.

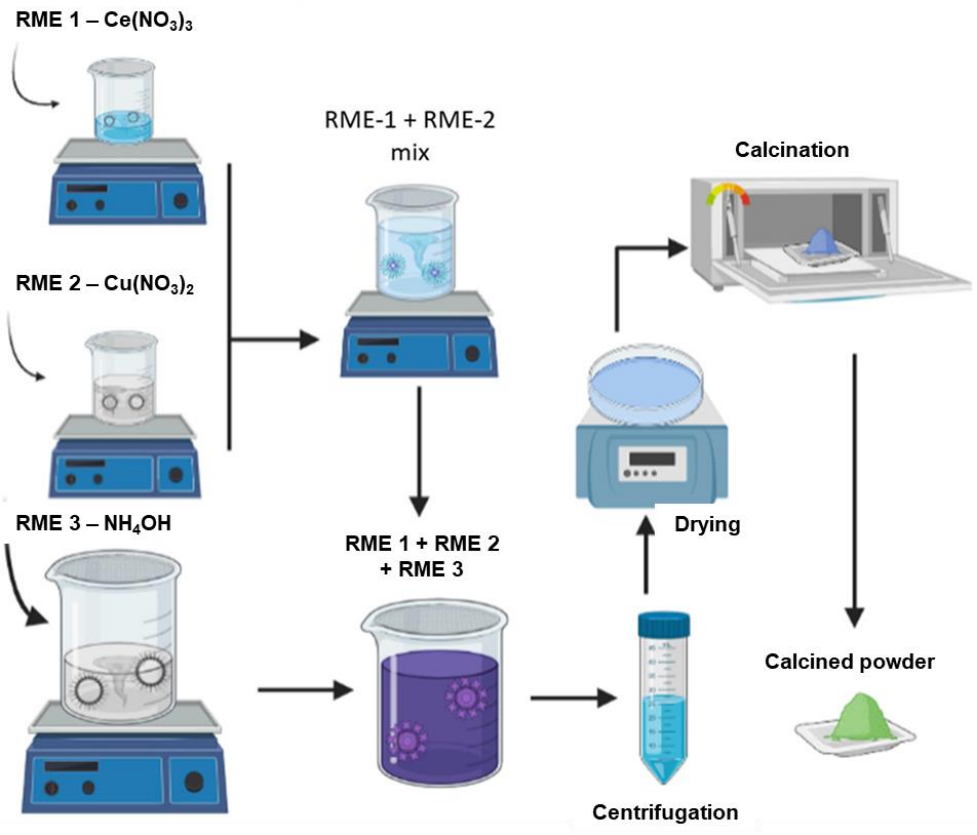

Figure 8. RME Synthesis schematic for $CuCeO_2$ catalyst preparation

The following steps were carried out for the synthesis of $CuCeO_2$ catalyst. Three different blank RME solutions were prepared for this catalyst. The blank RME was prepared by adding surfactant (Triton X-100, Acros Organics), a co-surfactant (propanol-2, Sigma-Aldrich) and an oil phase (cyclohexane, Sigma-Aldrich) in the ratio of 1:4.5:3.5 while under constant stirring. Once the blank RME are prepared, the aqueous phase for each RME was prepared. The aqueous phase was prepared by taking the respective salts for each RME and dissolving it in deionized water. The concentration of the aqueous phase was kept constant at 0.29M for all three RME solution. The ratio of aqueous for the aqueous phase, surfactant, a co-surfactant and an oil phase was 1:1:4.5:3.5. The volume of each constituent of the RME solution was calculated using analytical chemistry calculations.

The volume required to make 2g of 10.20 at% $CuCeO_2$ (at% denotes atomic percentage calculated as Cu/(Cu +Ce)) is shown in **Table 1.** The three different aqueous phase used were cerium nitrate (99.5% $Ce(NO_3)_3 \cdot 6H_2O$, Alfa Aesar), copper nitrate ($CuNO_3 \cdot 9H_2O$, Sigma-Aldrich), and ammonium hydroxide (28-30% NH_4OH, LabChem Inc.)), and were named as RME 1, RME 2 and RME 3 respectively. Once the salts are dissolved and the aqueous phase is ready, the aqueous phase is then poured into the blank RME solution dropwise under constant stirring. After 15 minutes of stirring, RME 2 ($CuNO_3 \cdot 9H_2O$) was added dropwise into RME 1 and was stirred for another hour to ensure molecular mixing of copper and cerium ions. Finally, for the precipitation to occur, RME 3 was added dropwise to RME 1 + RME 2 under continuous stirring and was allowed to react for 2h under continuous stirring. The ammonia hydroxide in RME 3 initiated the precipitation reaction for the $CuCeO_2$ catalyst to be formed. The solution was added dropwise to prevent agglomeration of particles and synthesize uniform nanoparticles **Figure 9** shows that RME 1 and RME 2 are light yellow and blue as $Ce(NO_3)_3$ and $CuNO_3$ yield those colours respectively. When RME 1, RME 2 and RME 3 were added together, the colour of the solution is initially a dark blueish green, however as the reaction progresses the colour becomes pale green.

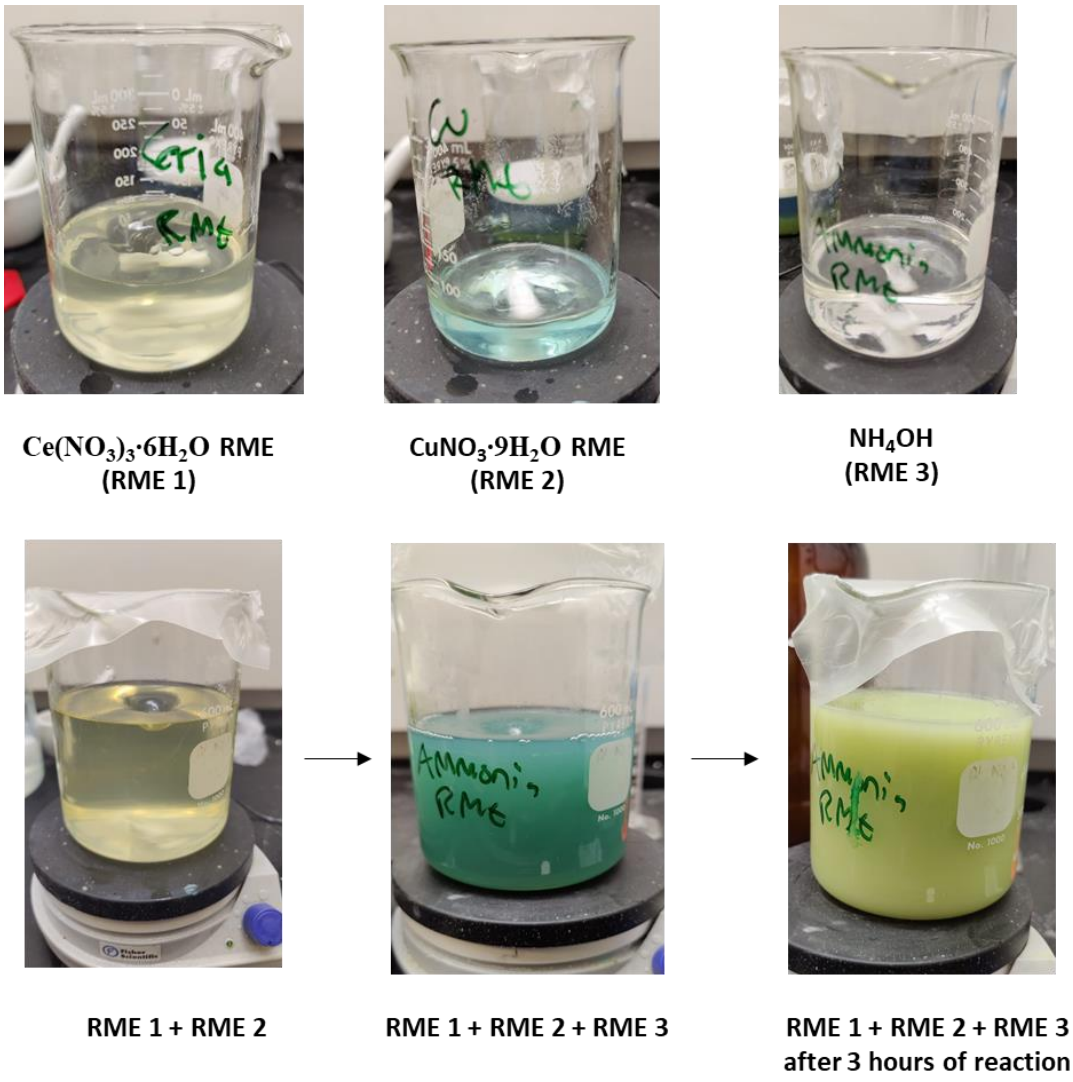

Figure 9. RME solution preparation procedure for synthesizing $CuCeO_2$ catalyst

Once the reaction was completed the mixture was left overnight to let the precipitate settle. After the supernate was removed, the precipitate was washed three times with deionized water, followed by centrifugation at 3500 RPM for 10 mins. The washed precipitate was transferred to a petri dish and dried at 150°C overnight on a heating plate. The dried precipitate was collected the next day and grounded to fine powder after which it was calcined at 275 °C under continuous flow of air in a muffle furnace for 4 h. The aforementioned procedures are shown in **Figure 10.**

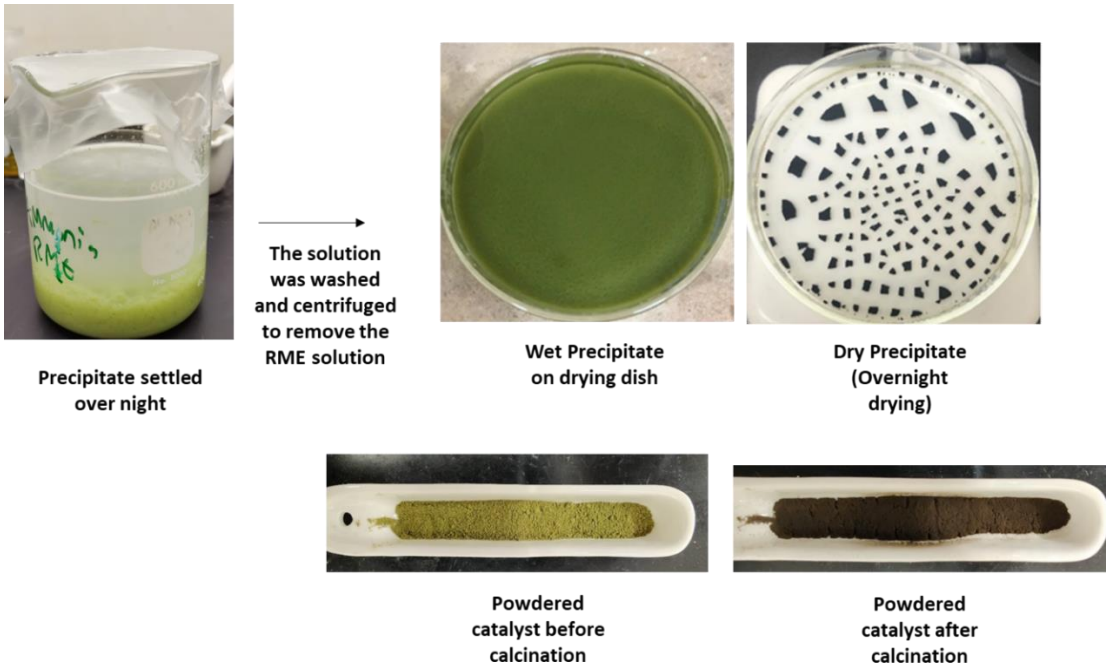

Figure 10. Drying and calcination preparation procedure for synthesizing $CuCeO_2$ catalyst

Table 1. Volume of different RME constituents required to make 10 at% $CuCeO_2$ catalyst

	Volume ratio	**RME 1: $Ce(NO_3)_3{\cdot}6H_2O$,**	**RME 2: $CuNO_3{\cdot}9H_2O$,**	**RME 3: 28-30% NH_4OH**
Aqueous phase (ml)	1	4.995g of $Ce(NO_3)_3{\cdot}6H_2O$, *40 ml solution*	0.6g of $CuNO_3{\cdot}9H_2O$, *8.6ml solution*	28-30% NH_4OH, *48.6ml*
surfactant	1	Triton X-100, *40ml*	Triton X-100, *8.6ml*	Triton X-100, *48.6ml*
Co-surfactant	4.5	Propanol-2, *180ml*	Propanol-2, *40ml*	Propanol-2, *220ml*

Oil phase	3.5	Cyclohexane, *140ml*	Cyclohexane, *30ml*	Cyclohexane, *170ml*

A similar procedure was done for $CeO_2/\gamma\text{-}Al_2O_3$ as well. Pure CeO_2 and three $CeO_2/\gamma\text{-}Al_2O_3$ catalysts (target values of 20, 30, and 40wt% CeO_2) were synthesized using the reverse microemulsion (RME) method. In the $CeO_2/\gamma\text{-}Al_2O_3$ synthesis, three blank RMEs were initially prepared by mixing Triton X-100 (Acros Organics), 2-propanol (Sigma-Aldrich Inc.), and cyclohexane (Sigma-Aldrich Inc.) in a specified ratio of 1:4.5:3.5, respectively. Calculated amounts of $Ce(NO_3)_3{\cdot}6H_2O$ (Alfa Aesar) and $Al(NO_3)_3{\cdot}9H_2O$ (Fisher Scientific) were dissolved in deionized water to form 0.29 M and 1 M aqueous solutions, respectively. These aqueous solutions (containing Ce and Al) precursors, as well as NH_4OH solution (14.8 M (28-30 wt%), LabChem Inc.) were added (separately) to a blank RME to prepare three RMEs, each one containing either $Ce(NO_3)_3$, $Al(NO_3)_3$, or NH_4OH (denoted as Ce-RME, Al-RME, and NH_4-RME).

For $CeO_2/\gamma\text{-}Al_2O_3$ catalysts, Al-RME was dropwise added to NH_4-RME under vigorous stirring and left under stirring for 1 h. After 1 h stirring, Ce-RME was added dropwise. Upon addition of Ce-RME, the mixture turned to light yellowish-brown, and then, after 1 h of mixing, to bright yellow, indicating the formation of cerium oxide (**Figure 11**). For the bulk CeO_2 catalyst, NH_4-RME was added to Ce-RME dropwise under stirring and left under stirring for 1h. The mixtures were left overnight (12 h) for precipitation and sedimentation. After this, the process is the same as $CuCeO_2$ (washing the precipitate, drying and calcination a 275°C for 4 hours).

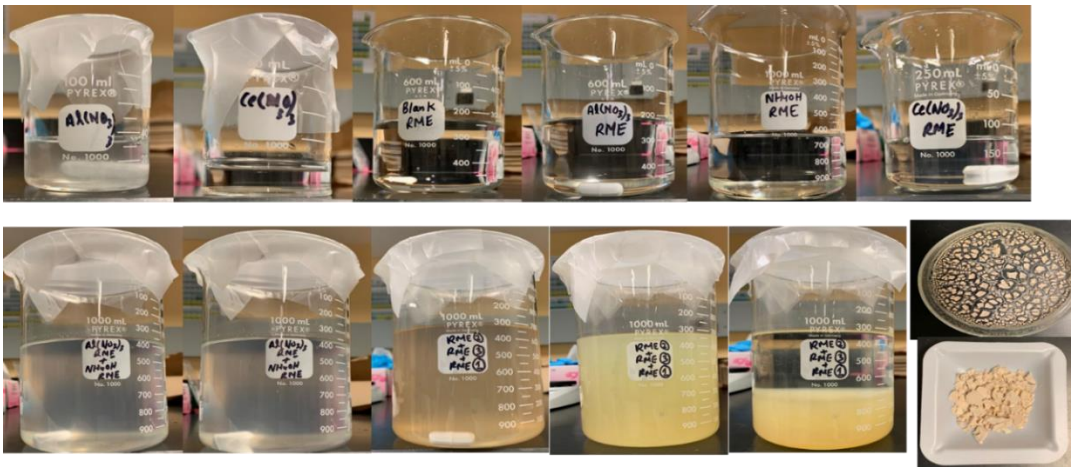

Figure 11. $CeO_2/\gamma\text{-}Al_2O_3$ catalyst preparation sequence

3.2 Experimental techniques

In this section, all analytical techniques used in this study are briefly presented with its fundamental principles and schematics (if applicable). These methods are used to evaluate the catalyst composition, morphology and performance

3.2.1 X-Ray powder diffraction (XRD)

XRD is a nondestructive analytical tool that is used to identify the chemical components and the crystal structure of the existing phases in XRD. When a beam of X-ray passes through the crystal phase of an atom, the X-ray beam is diffracted. The diffracted X-ray generates a pattern that reveals the structural orientation of each atom in a given compound.

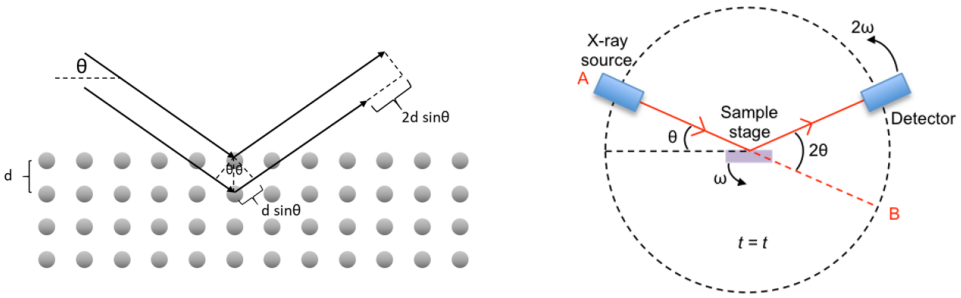

Figure 12. (left) Bragg's law, (right) schematic of a typical XRD measurement

XRD relies on the constructive and destructive interference of monochromatic X-rays when passing through a crystalline sample. By using a cathode ray tube, monochromatic X-rays are generated and filtered to emit radiation of a single wavelength. These X-rays are then collimated and directed towards the sample. The detector and the sample stage move with a certain circular speed such that they can always satisfy 2θ angle for Bragg's law. When the conditions satisfy Bragg's law ($2d\sin\theta = n\lambda$, where λ represents the X-ray wavelength, n is a positive integer, d is the plane spacing, and θ is the grazing angle), constructive interference occurs through the interaction between the sample and the incident rays **(Figure 12)**. Analyzing the diffraction pattern obtained on a photographic film allows for the determination of the crystal structure. When X-rays meet the conditions outlined in the aforementioned equation, a superposition is observed in the direction of reflection. This means that each crystalline plane will have its own peak position and intensities, which can be compared with literature to identify the sample composition. By initially measuring the diffraction wave's angle (θ) for a known crystal, the X-ray's wavelength can be calculated, enabling the identification of the element responsible for generating the characteristic X-ray.

X-ray diffraction (XRD) patterns were obtained using Rigaku MiniFlex II and analyzed using Bruker EVA software. Crystallite size was calculated using Bruker EVA software from Scherrer equation, Eq. (4).

$$D_{XRD} = \frac{K\lambda}{\beta \cos\theta} \tag{4}$$

3.2.2 Inductively coupled plasma optical emission spectrometry (ICP-OES)

ICP-OES is a technique primarily used to analyze the concentrations of elements in different samples. It is a widely used technique in various industries, such as the environmental, and pharmaceutical industries, due to its rapid multiple elemental analysis with much higher sensitivities like parts per billion (ppb) to parts per million (ppm) [36]. The fundamental principle of ICP relies on quantized level of energy structure for the ions and atoms. When an atom or ion in its lowest energy state (ground state) absorbs external energy, its electrons move to higher energy levels. However, atoms or ions in the excited state are highly unstable and will transition back to the ground state, emitting the absorbed energy in the form of electromagnetic waves [37]. The wavelengths of these waves generated by excited atoms vary. Due to the presence of multiple energy levels in atoms or ions, specific elements can produce characteristic spectra consisting of various wavelengths. Analyzing these spectra provides valuable information about the elements present.

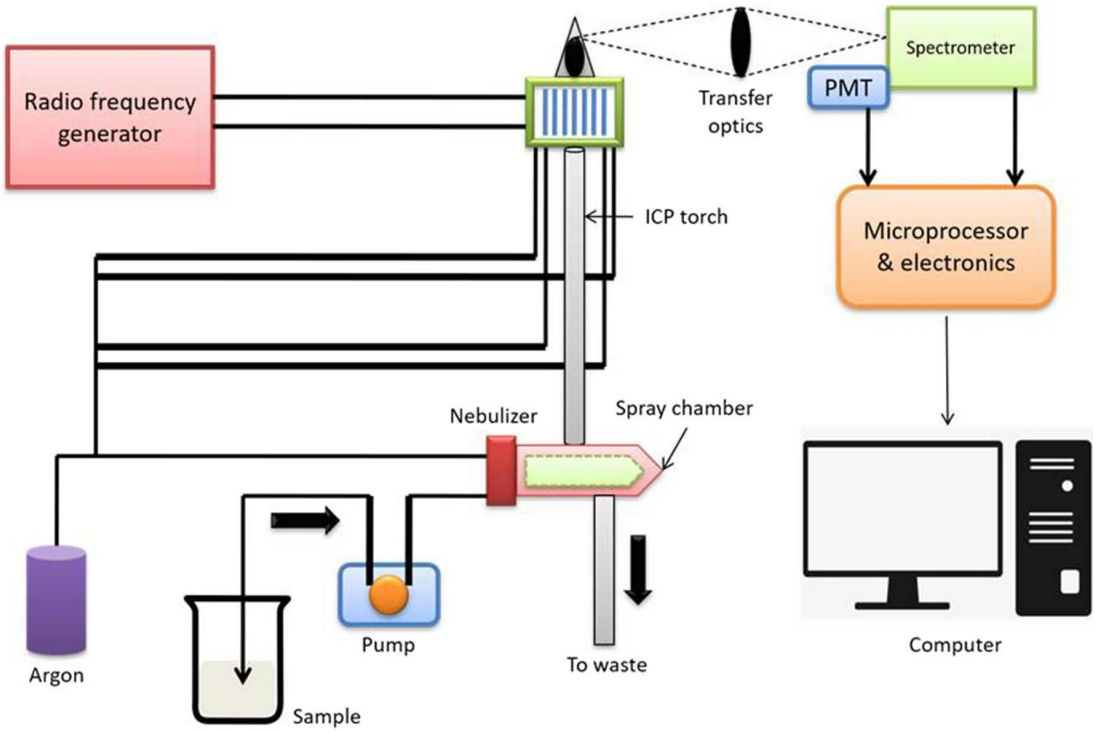

Figure 13. Schematic of an ICP-OES Instrumentation [37]

Figure 13 shows a schematic of ICP-OES. In ICP-OES, the sample goes is pumped through a nebulizer where liquid samples are transformed in an aerosol. This aerosol is then introduced to an argon plasma (ICP torch) where it is ionized. The samples under goes excitation and relaxation, which releases photons. These photons are collected with the help of concave mirror to the sensor and analyzed. This information is used to determine the element present and the concentration of that element present in a given sample [37].

3.2.3 X-ray photoelectron spectroscopy (XPS)

X-ray photoelectron spectroscopy (XPS) is a surface chemical analysis that can be used to study the chemical state present on the surface of a sample. In XPS analysis, samples are irradiated with X-Ray beams on the sample which results in transfer of x-ray energy to a core level electron. The kinetic energy of the emitted electrons (KE), binding energy of the electron to the atom (BE), and the energy of the x-ray are expressed in the following

equation $BE = hv - KE - \Phi_{spec}$ where Φ_{spec} is the spectrometer work function[38]. Photoelectron peaks are unique to an element and the orbital from which it is emitted. Due to this, XPS can be used to identify both the element and the chemical state of the element. XPS spectra were recorded on a ESCALAB 250Xi Microprobe system (Thermo-VG Scientific) equipped with a hemispherical analyzer and a monochromatic Al Kα X-ray source (1486.6 eV). All measurements were done at room temperature with a background pressure of less than 5×10^{-10} mbar.

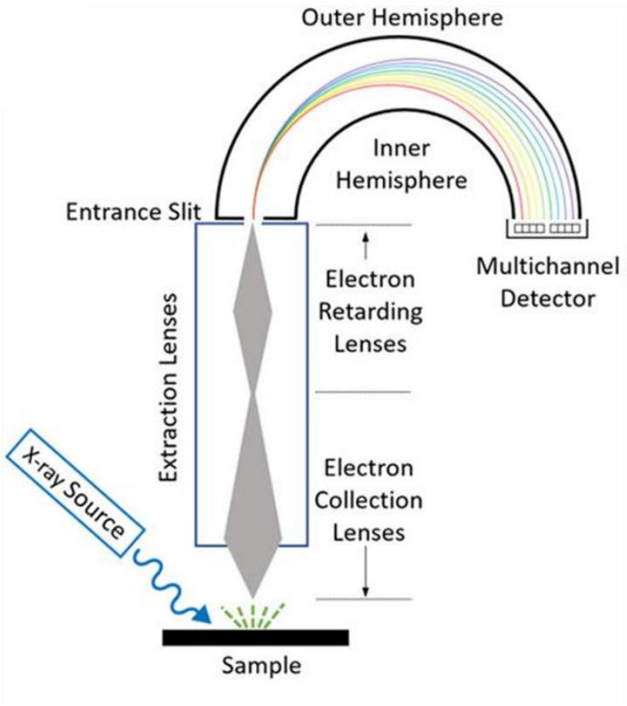

Figure 14. Schematic diagram of a XPS instrument [38]

The schematic of a XPS instrument is shown in **Figure 14.** The sample is placed in the holder where the X-ray can hit the sample. The X-Ray source used in this project is monochromatic Al Kα x-ray. Between the sample and analyzer, there are a series of lenses that help with detecting the emitted electrons. The lenses help reduce the speed of the electrons travelling to the detector as this allows for a higher energy resolution [38]. Once

it is retarded, it is then detected and processed by the instrument. The instrument is operated at ultra-high vacuum to prevent emitted electrons from interacting with air molecules and reducing any surface contamination [38].

3.2.4 Brunauer Emmett Teller (BET) Specific Surface Area (SSA)

The surface area of a catalyst is a crucial factor influencing its performance, thus necessitating accurate measurement. Brunauer Emmett Teller (BET) method relies on the adsorption isotherms (amount adsorbed on the solid against the equilibrium pressure) of non-reactive gas molecules that covers the monolayer coverage of the molecule. [39]

The BET model, represented by **Eq. 5** involves several parameters: p (pressure at equilibrium), p_0 (saturated vapor pressure of the adsorbed gas at the given temperature), Vm (volume of gas required to form a monolayer on the surface), V (amount of adsorption at pressure p), and C (a constant) [40].

By acquiring a set of p and V values, a plot of $p/V(p_0-p)$ against p/p_0 can be generated, resulting in a linear relationship. The slope of this line corresponds to (C-1) / CVm, and the intercept represents 1 / CVm, enabling the determination of Vm and the constant C. Utilizing **Eq. 6**, which relates to surface area, it becomes possible to calculate the specific surface area. The equation incorporates NA (Avogadro constant), s (adsorption cross-sectional area of the adsorbed species), V (molar volume of the adsorbed species), and a (quality of the adsorbent material) [40].

$$\frac{P}{V(p_0-p)} = \frac{1}{V_m C} + \frac{C-1}{V_m C} \times \frac{p}{p_0} \quad (5)$$

$$S_{BET} = \frac{(V_m N_A s)}{V} \quad (6)$$

The adsorption isotherms are measured at lower temperature to prevent any chemical adsorption on the surface of the catalyst which is the reason why liquid nitrogen is used to bring the temperature down. A typical operation of BET typically consists of heating the sample to a 300°C under an inert gas to remove a volatile substance. After the volatile substances are removed, sample is cooled with liquid nitrogen to around -190°C. During this step, the samples is subjected to N_2 flow where it is subjected to different pressure. The variable pressure is achieved by changing the amount of gas adsorbed on the surface of the catalyst. The resulting isotherm is then plotted using Eq 6. SSA was determined AMI-300Lite, Altamira Instruments using 10% N_2/He as adsorbing gas

3.2.5 Thermogravimetric analysis (TGA)

Thermogravimetric analysis (TGA) is a useful analytical tool that is used to study material stability, decomposition kinetics and product lifetime. TGA measures the relationship between the mass and temperature of a given sample by heating the sample at a constant rate. TGA has a very high accuracy balance and as such. analyzing the thermogravimetric curve (weight vs temperature) can give information on thermal stability and product formation on a sample.

For this project, TGA was used to evaluate the extent of coking on the catalyst. TGA was connected in-line with a FTIR to also measure the evolved gases when the sample is heated. TGA curve combined with the evolved gases measured through FTIR was used to analyze the extent of coking on catalyst. **Figure 15** shows a typical schematic for TGA. The sample is suspended with a balance weight for high accuracy measurements. TGA instrument was brought to an equilibrium temperature of 25°C and maintained in an isothermal condition for 10 minutes. Subsequently, the sample was heated to 150°C at a

rate of 10°C per minute after which the sample was heated from 150°C - 800°C, using a ramping rate of 2°C and an airflow rate of 40 ml/min. Throughout the combustion process, the outlet gases from the TGA were directed towards the FTIR gas analyzer to detect the presence of CO_2 and CO. Thermal gravimetric analysis (TGA) was conducted on TGA 55 (TA Instruments), using the continuous flow FTIR analyzer (MultiGas^{TM} 2030, MKS Instruments) for off-gas analysis.

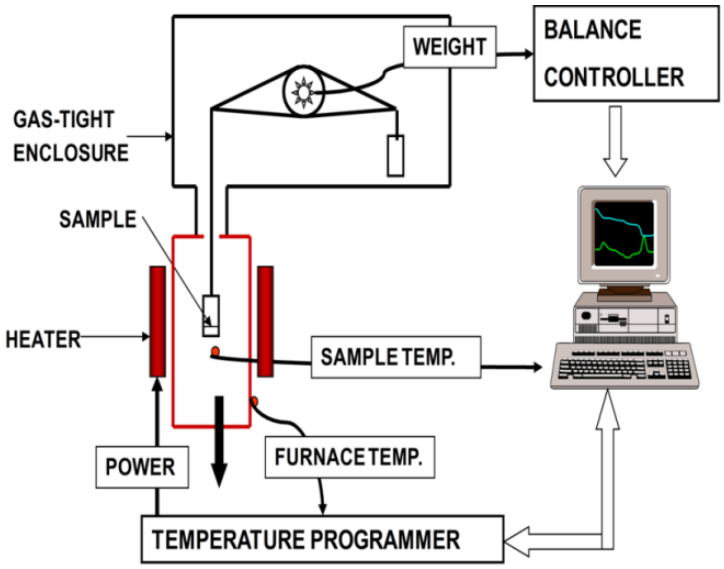

Figure 15. TGA Apparatus schematic [41]

3.2.7 CO_2 Temperature programmed desorption (TPD)

Temperature programmed desorption (TPD) are a useful technique to evaluate interaction between CO_2 and the surface of the catalyst. TPD can help identify the number of active sites and calculate strength of active sites. The TPD peaks can be used to calculate the activation energy of desorption (discussed later) of a catalyst as well.

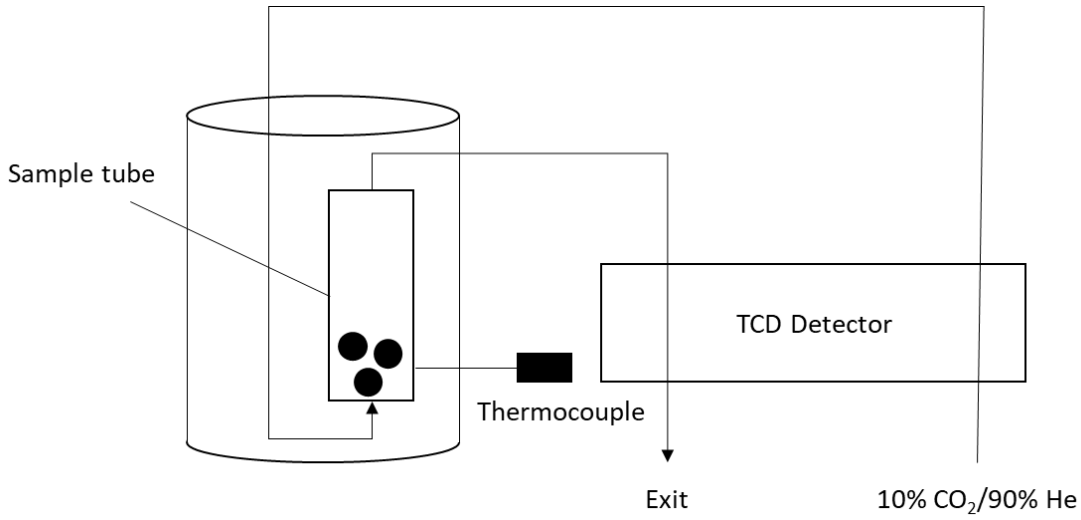

Figure 16. CO_2 TPD schematic

Figure 16 shows the CO_2 TPD schematic. In a typical TPD experiment, low concentration CO_2 balanced with inert gas (e.g. 5% CO_2/He) is flushed on the surface at room temperature for surface adsorption. Subsequently the sample bed is heated at a constant heat rate until of 600°C. As the temperature increases, the adsorbed species desorb when the thermal energy is greater than the adsorption energy. To detect and analyze the desorbed gas, a Thermal Conductivity Detector (TCD) is employed. The TCD allows for the monitoring of the desorption events and provides a TPD curve which with desorption peaks. This information can be used to assess the nature of active sites on the surface of the catalyst.

For CO_2-TPD in this project, 0.1g of catalyst was reduced in 10% H_2/Ar at 400°C for 2 hours. The sample was flushed with helium (He), until it was cooled down to room temperature. Then, the catalyst was exposed to 5% CO_2/He for 1 hour followed by He flush. The TPD analysis was carried out by heating from 25°C - 600°C under He at a heating rate of 5°C/min.

Activation energy of desorption was calculated using Eq 5. using the Polanyi-Wigner equation where T_{max} is peak temperature from TPD, β is the TPD heating rate, R is the gas constant and v_1 is the frequency factor. A redhead analysis was conducted where the following assumptions were made: activation parameters are independent of surface coverage and the desorption follows 1st order kinetics. [42]

$$\Delta E_{des} = RT_{\max}\left[\ln\frac{v_1 \cdot T_{\max}}{\beta} - \ln\frac{\Delta E_{des}}{RT_{\max}}\right] \tag{7}$$

3.3 Flow system and reaction test

3.3.1 Flow system configuration

The reactor system **(Figure 17)** comprises of a programmable Muffle Furnace (KSL-1100X Muffle Furnace, MTI Corporation) where the reactor is placed. A K type thermocouple (1/8″, Omega Engineering) was inserted through the outlet tube so that the thermocouple tip is in contact with the catalyst bed (**Figure 18**). Mass flow controllers (EL-FLOW select mass flow controllers, HOSKIN SCIENTIFIC LIMITED) were used to control feed flow rates and pressure was controlled using a mechanical back pressure regulator (Stainless Steel BP Regulator, Swagelok). Water was removed using a mist trap (SMC AFM40-N02-Z-A, SMC Corporation) and a silica gel column (Agilent Technologies, 5182-9411, filled with silica gel orange, Fisher Scientific). Concentrations of CO, CO_2 and CH_4 in the outlet stream were measured on a dry basis with the IR analyzer (IR-208, Infrared Industries, Inc., USA). The entire flow system was computer-controlled using LabVIEW (National Instruments), with the flow rates, pressure, temperature and gas concentrations being continuously monitored and recorded using analog-to-digital converters (NI 9215, NI 9263, National Instruments).

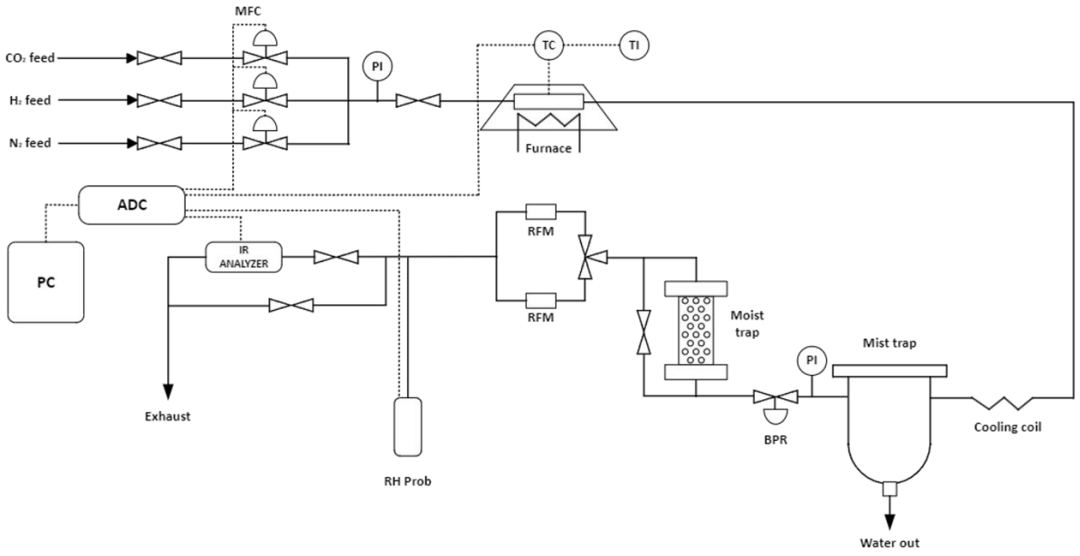

Figure 17. Flow system setup for conducting catalytic performance evaluation. Abbreviations: ADC, analog-to-digital converter; BPR, back pressure regulator; RFM, Rotor flow meter ; IR, infrared; MFC, mass flow controller; PI, pressure indicator; PC, personal computer; TC, thermocouple; TI, temperature indicator.

3.3.2 Reactor configuration

For reaction tests, a stainless steel (SS) 1/4" tube was used **(Figure 18)**. Pelletized and sieved catalysts (350-450 µm particle size) were loaded into the reactor through the either side of the SS tube sandwiched by quartz wool on both sides. Post reaction, the catalyst is then removed by removing the quartz wool for post reaction characterization test.

For stability tests, a 1/4" U-shaped quartz reactor was connected to SS flexible tubing and connected to the flow system. 400 mg of pelletized and sieved catalyst (350-450 µm) was fixed inside the reactor between quartz wool, then the reactor was placed inside the furnace.

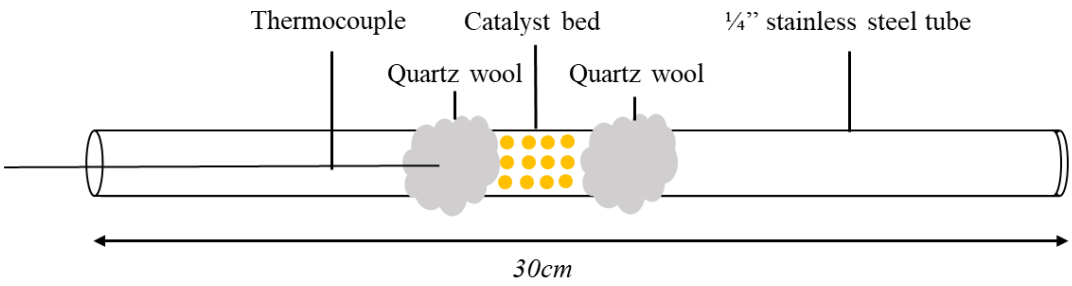

Figure 18. Stainless steel reactor schematic used for reaction tests

3.3.3 Reaction test and operating conditions

Prior to reaction tests, all catalysts were reduced under H_2 (200 mL/min at 600 °C for 2 h). After reduction, the feed was switched to a 3:1 mixture of H_2 and CO_2, and the temperature was reduced stepwise (50 °C step) in the 600-300 °C range (hold at 600 °C in the stability test). The duration of each step was 3 h to allow for complete stabilization of the IR signals for each temperature. All reported conversion and selectivity values were calculated under steady-state conditions (except for the stability test where transient data is reported).

CO_2 conversion and selectivity to CO were calculated according to Eqs. (8, 9) (y_{CO}, y_{CH_4}, and y_{CO_2} are mole fractions on dry basis, after removal of condensed water and humidity).

$$X_{CO_2} = \frac{y_{CO} + y_{CH_4}}{y_{CO_2} + y_{CO} + y_{CH_4}} \quad (8)$$

$$S_{CO} = \frac{y_{CO}}{y_{CO} + y_{CH_4}} \quad (9)$$

Carbon balance of the system is given by **Eq. (10)**. Where, α is the ratio of H_2/CO_2 in the feed, f_1 and f_2 are the conversion to CO and CH_4 respectively, $F_{C,out}$ is the outlet molar flow rate [43].

$$CB = (y_{CO_2} + y_{CO} + y_{CH_4})(1 + \alpha - f_1 - 4f_2) \tag{10}$$

$$\alpha = \frac{F_{H_{2,f}}}{F_{CO_{2,f}}} \tag{11}$$

$$f_1 = \frac{y_{CO}}{y_{CO_2} + y_{CO} + y_{CH_4}} \equiv \frac{F_{CO,out}}{F_{C,out}} = \frac{F_{CO,out}}{F_{CO_2,f}} \tag{12}$$

$$f_2 = \frac{y_{CH_4}}{y_{CO_2} + y_{CO} + y_{CH_4}} \equiv \frac{F_{CH_4,out}}{F_{C,out}} = \frac{F_{CH_4,out}}{F_{CO_2,f}} \tag{13}$$

Turnover frequency was calculated from **Eq. 16,** where M_w is the molar mass of CeO_2, D is dispersion, and R_{max} is the maximum value of the CO_2 conversion rate (R) obtained at high space velocities; R is calculated using **Eq. (14)** $F_{CO_2,f}$ is feed rate and W_c is catalyst weight). Dispersion (D) was calculated using **Eq. (15)**, where N_a, ρ_p, A_s, and D_{XRD} are Avogadro's number, bed density(1.438 g/ml, assuming CeO_2), single adsorption site surface area (1.961nm^2 [44]), and crystallite size as calculated using Scherrer equation (Eq. 3).

$$R = \frac{F_{CO_2,f} X_{CO_2}}{W_c} \tag{14}$$

$$D = \frac{6M_W}{N_A \rho_p A_s D_{XRD}} \tag{15}$$

$$TOF = \frac{M_W}{D} R_{\max} \tag{16}$$

Chapter 4: Hindering CeO_2 nanoparticle growth in CeO_2/γ-Al_2O_3 catalyst

4.1. Catalytic performance evaluation

To validate CeO_2 loading, ICP-OES was conducted for fresh catalysts (after calcination). The results are summarized in **Table 2**, alongside specific surface area (SSA) for fresh and spent (post-reaction, after 70 h on stream) catalysts. CeO_2 loadings showed relatively small deviations from target values, except for the highest target loading (40 wt%). These deviations can be attributed to lower degree of precipitation for γ-Al_2O_3 as compared to CeO_2, with unprecipitated ions being washed out during washing step (see *Section 3.1*). Please, note that in the discussion below catalyst are denoted according to their target loading, i.e., 20, 30, and 40wt% CeO_2.

Table 2: CeO_2 loadings (as measured by ICP-OES) and specific surface area (for fresh and spent catalysts).

Sample	**CeO_2, wt%**	**SSA, m^2/g**	
		fresh	***spent***
20wt% CeO_2	20.2	310.0	158.3
30wt% CeO_2	34.1	299.7	105.4
40wt% CeO_2	47.9	292.1	97.6
CeO_2	100	146.8	38.7

The specific surface area of 20wt% CeO_2 was the highest, with a value of 310 m^2/g, and it decreased as the CeO_2 loading increased. Similar trend was observed by Damyanova et al. [45], showing that at higher CeO_2 loadings specific surface area decreases due to the plugging of the pores of γ-Al_2O_3 with CeO_2 nanoparticles. Notably, there is a substantial

reduction in SSA under reaction conditions, for CeO_2 in particular (73.6% SSA reduction vs. 48.9-66.6% for CeO_2/γ-Al_2O_3 samples). It should be noted that all samples were calcined at a relatively low temperature (275 °C) before reaction tests which were conducted at 300-600 °C. A more detailed analysis of SSA reduction and discussion is provided later (*Section 4.3*).

In all reaction tests, catalysts were reduced under the flow of pure H_2 (100 mL/min) for 2 h at 600 °C prior to switching to reactive feed (CO_2/H_2 mixture). The H_2/CO_2 feed ratio was kept constant at 3, while pressure was held at 3 bar (absolute pressure) for all experiments. Catalyst performance for pure CeO_2 (denoted as CeO_2 further in the text) and 20, 30, 40wt% CeO_2/γ-Al_2O_3 (denoted as 20wt% CeO_2, 30wt% CeO_2 and 40wt% CeO_2, respectively) was first evaluated in the temperature range of 300-600 °C, at a fixed space velocity of 60,000 ml/(g h). For each temperature or space velocity step, the step duration was 2 h at least and all values were recorded after complete stabilization of the IR signals.

Figure 19a shows CO_2 conversion and CO selectivity calculated by Eqs. **(8-9)** as a function of temperature. All catalysts were 100% selective to CO formation. It was previously reported that pure CeO_2 can show complete selectivity to CO formation [23]. Still, the observation of complete CO selectivity for CeO_2/γ-Al_2O_3 is important as it indicates that the active-phase support interaction does not change the reaction mechanism. Conversion was only detectable at 400 °C for all catalysts and increased with temperature. The 20wt% CeO_2 catalyst showed the lowest conversion in the entire temperature range. Other catalysts had very similar CO_2 conversion in the temperature range of 400-550 °C, with some relatively significant differences at 600 °C. CeO_2 showed the highest conversion at 600 °C with a conversion value of 0.42, closely followed by 40wt% CeO_2 with a

conversion value of 0.37. The observation of virtually identical CO_2 conversion for 30wt% and 40wt% CeO_2 as compared to bulk CeO_2 is indicative of similar amounts of exposed active sites, which can be in theory obtained via better dispersion, i.e., smaller CeO_2 nanoparticle size with less agglomeration for CeO_2/γ-Al_2O_3 samples.

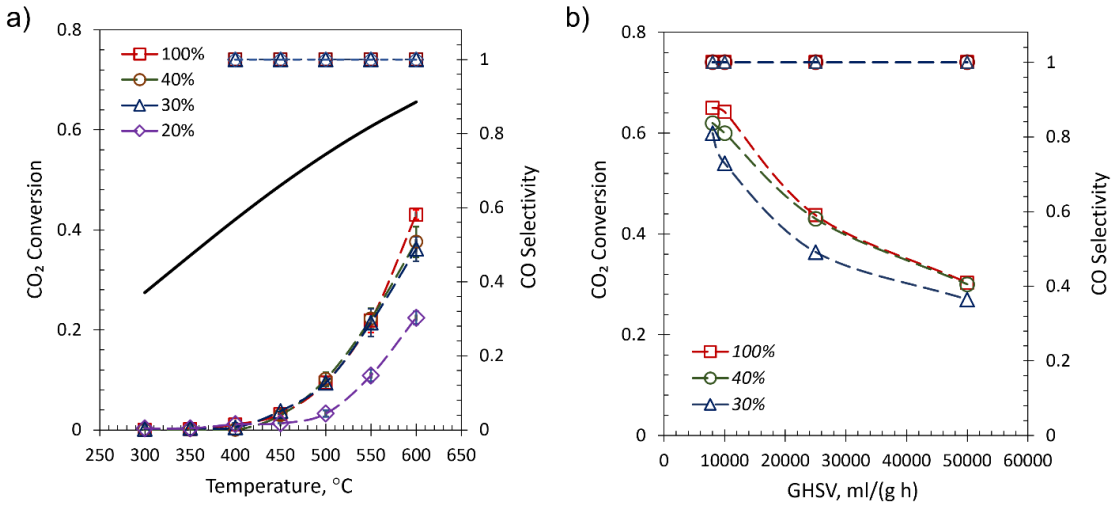

Figure 19. Catalytic performance evaluation as a function of temperature (300-600°C) (a) and GHSV (8,000 – 50,000 ml/(g h)) (b). The black solid line represents RWGS equilibrium. Parameters: P = 3 bar, H_2/CO_2 = 3 (feed), GHSV = 60,000 mL/(g h) (a), T = 600 °C (b).

To further investigate the catalytic performance, reaction tests were conducted at 600 °C in the range of space velocities (8,000-50,000 mL/(g h)) (**Figure 19b**). Similarly to the previous experiment, CO selectivity remained 100% in the entire range of space velocities for all catalysts, indicating again that the reaction mechanism is not affected by the active phase-support interaction. All catalysts performed significantly better at lower GHSV, which is a typical behavior (at higher space velocities conversion is limited by shorter residence times and insufficient amounts of available sites). CeO_2 showed a nearly equilibrium conversion of 65% at 8,000 mL/(g h), while 40wt% CeO_2 showed a very

similar performance attaining 60% conversion at 8,000 mL/(g h). 30wt% CeO_2 showed substantially lower conversion in the entire range, which can be attributed to the lower amount of exposed active sites. It should be emphasized at this point that it is preferable to scan over ranges of both temperature and space velocity for more comprehensive catalytic performance evaluation.

Figure 20 shows CO generation rates calculated by **Eq. (17)** and corresponding Arrhenius plots, which were used to estimate activation energies by **Eq. (18)**.

$$R_{CO} = \frac{F_{CO_2,f} \times X_{CO_2}}{W_C} \tag{17}$$

$$\ln(R) = \ln(A) - \frac{E_a}{R_g T} \tag{18}$$

The CO generation rate was the lowest for the 20wt% CeO_2 catalyst, while other catalysts showed similar generation rates, in accordance with the data reported in **Figure 19a**. Activation energy estimation showed that CeO_2 and 40wt% CeO_2 have similar activation energies, of 100.0 and 97.3 kJ mol^{-1}, respectively. For 30wt% CeO_2 and 20wt% CeO_2 activation energies were substantially lower, 89.2 and 77.8 kJ mol^{-1}, respectively. It is interesting that the activation energy decreased monotonically (but not linearly) with decreased CeO_2 loading, indicating that the degree of dispersion and active phase-support interaction affect the catalytic activity. Although the activation energy for 20wt% CeO_2 was substantially lower, this activity enhancement was not significant enough to overcome the limiting amount of the exposed active sites as compared to higher CeO_2 loadings and pure CeO_2. As a result, the CO generation rate was significantly lower for 20wt% CeO_2. It is worth mentioning that other catalytic systems can demonstrate opposite behavior, i.e.,

different performance for similar activation energies. E.g., Panagiotopoulou et al. [46] evaluated TiO_2-supported noble metals (Pd, Pt, Ru, Rh) for water gas shift and found lower performance for Pd despite similar activation energies for all catalysts; this difference was attributed to metal-support interactions.

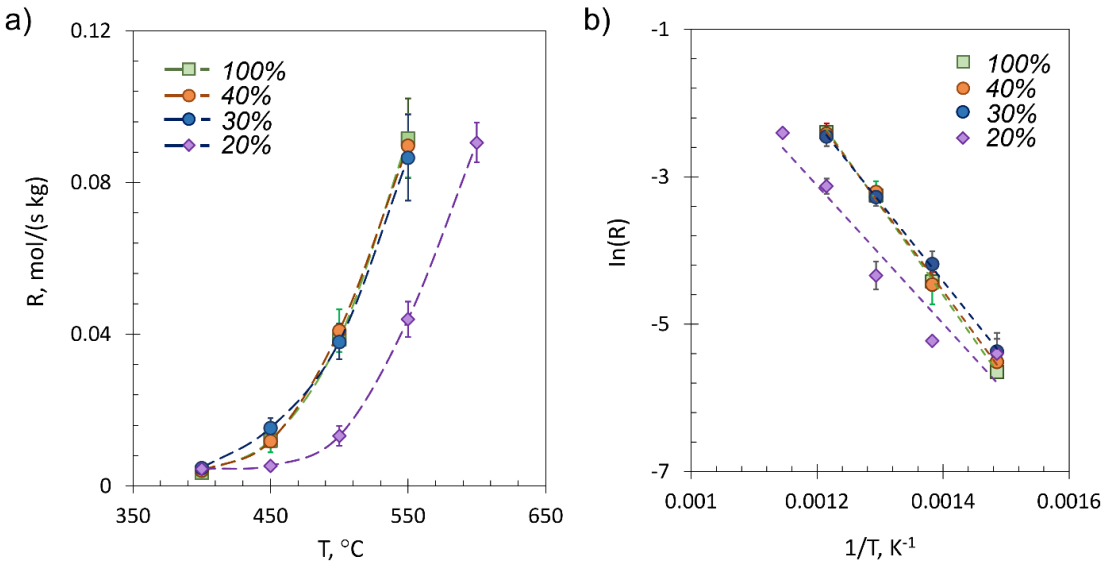

Figure 20. Rate of CO generation as a function of temperature at 60,000 ml/(g h) (a) and corresponding Arrhenius plots (b). 20, 30, 40, and 100% notation corresponds to 20, 30, 40wt% CeO_2, and pure CeO_2 samples.

Altogether, the obtained results of the catalytic performance evaluation indicated that the 40wt% CeO_2 catalyst performs very similarly to the unsupported (bulk) CeO_2, as evident from reaction tests in the range of both temperature and space velocity (**Figure 19**). It can also be concluded that the catalytic performance (in terms of CO_2 conversion and CO generation rate) increases with increasing CeO_2 loading. This is an expected but not trivial results, since catalytic performance is not exclusively affected by the amount of the active phase but also affected by other factors, such as active phase dispersion (nanoparticle

size and degree of agglomeration) and physicochemical characteristics of the catalytic surface (nanoparticles can have different shapes and facets).

To the best of authors' knowledge, implementation of CeO_2/γ-Al_2O_3 has not been reported in the literature yet. For other catalytic systems, it has been also shown that CeO_2/Al_2O_3 activity increases with the increase in CeO_2 loading. E.g., Guo et al. [47] evaluated CeO_2/Al_2O_3 for the catalytic reduction of NO with NH_3 and suggested that the interaction between CeO_2 and Al_2O_3 may lead to the formation of $CeAlO_3$, resulting in the Ce^{4+}-to-Ce^{3+} conversion, and subsequently leading to more oxygen vacancies. In another study, Martinez-Arias et al. [48] evaluated structural and redox properties of CeO_2 in the Al_2O_3-supported CeO_2 catalyst and concluded that at high CeO_2 loadings the catalyst consists primarily of aggregated crystalline CeO_2 species, thus presenting a chemical behavior more similar to an unsupported CeO_2.

4.2. Catalyst stability

Catalyst stability tests, which are often overlooked from studies of new catalytic materials, are very important, in particular for high-temperature reactions (such as RWGS) that can induce nanoparticle growth and sintering. For reactions involving carbonaceous species, it is also very important to evaluate the degree and type of coking, which can be severe under certain reaction conditions.

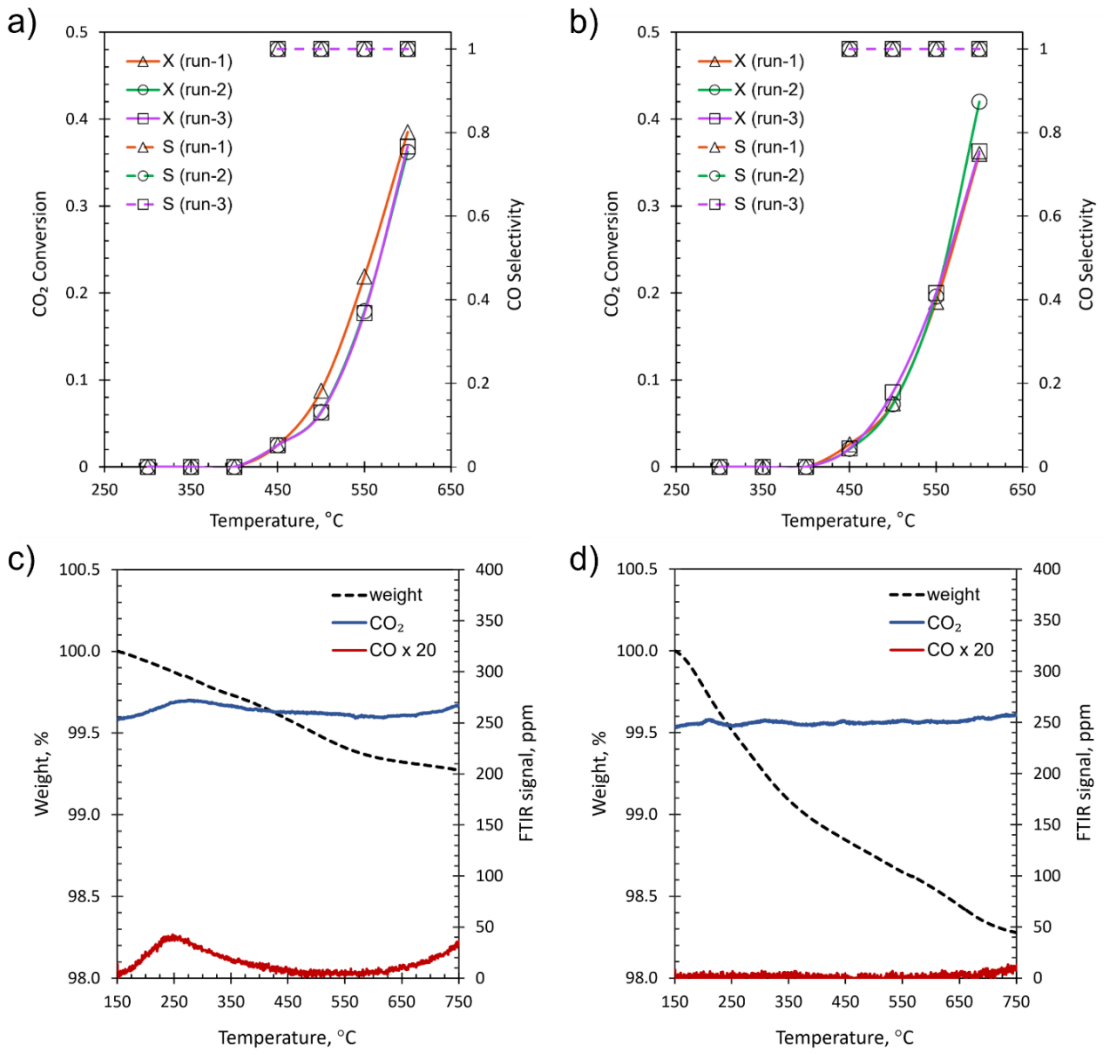

Figure 21. Reaction/cooling cycles for CeO_2 (a) and 40wt% CeO_2 (b). Corresponding TGA-FTIR analysis of spent catalysts are also shown for spent CeO_2 (c) and 40wt% CeO_2 (d).

First, repeatability was evaluated via a heating/cooling cycle experiment, under the same conditions as in the reaction test reported in **Figure 19a**. After each scan over the temperature range, the system was allowed to cool down to 300 °C under the flow of N_2 and then the experiment was repeated. **Figure 21** shows the results of cyclic tests for CeO_2 and 40wt% CeO_2, alongside TGA-FTIR analysis to evaluate the extent of coking. In terms

of CO_2 conversion and CO selectivity, both catalysts showed stable catalyst performance during three runs, with reasonably consistent conversion values and, importantly, complete selectivity to CO formation (**Figure 21a, b**).

To investigate the extent of coking, TGA-FTIR analysis was conducted for spent catalysts (CeO_2 and 40wt% CeO_2) recovered from the reactor after three reaction-cooling cycles. For the spent CeO_2 catalyst (**Figure 21c**), a minor weight loss of ca. 0.8% was observed. This weight loss was associated with weak, broad peaks of CO_2 and CO centered at ca. T = 250-260 °C. Since this minor weight loss was associated with carbonaceous species in the off-gas, it can be concluded that a small amount of polymeric or amorphous carbon was formed on the catalyst surface. For the 40wt% CeO_2 the observed weight loss was almost 2% (still insignificant), but no distinct peaks of either CO or CO_2 were detected. The lack of CO and CO_2 peaks indicates the absence of any carbonaceous species on the surface of the spent catalyst. Another possible explanation for the observed weight loss (not associated with coke) could be the loss of oxygen, as both CeO_2 and Al_2O_3 lose oxygen at elevated temperatures [49]. To sum up, only minor weight loss was observed for both catalysts, which is indicative of high resistance to coke formation (probably due to high reducibility of CeO_2 that can provide oxygen to oxidize carbonaceous species).

Next, stability tests were conducted for CeO_2 and 40wt% CeO_2 at a fixed temperature of 600 °C and two different space velocities of 60,000 ml/(g h) and 10,000 ml/(g h) (**Figure 22**). In these tests, a quartz reactor was used to rule out any possibility of metal dusting that can affect stainless steel reactor walls under prolonged exposure to CO/H_2 mixture. Both samples were 100% selective to CO throughout the entire duration of stability tests. For the pure CeO_2 catalyst, nearly equilibrium conversion was initially achieved at 10,000

ml/(g h) (63% vs. 65% equilibrium conversion), with a relatively minor decrease towards the end of the stability test (51%). At 60,000 ml/(g h), the decrease in conversion was more substantial throughout the duration of the experiment(from 33% to 24%).

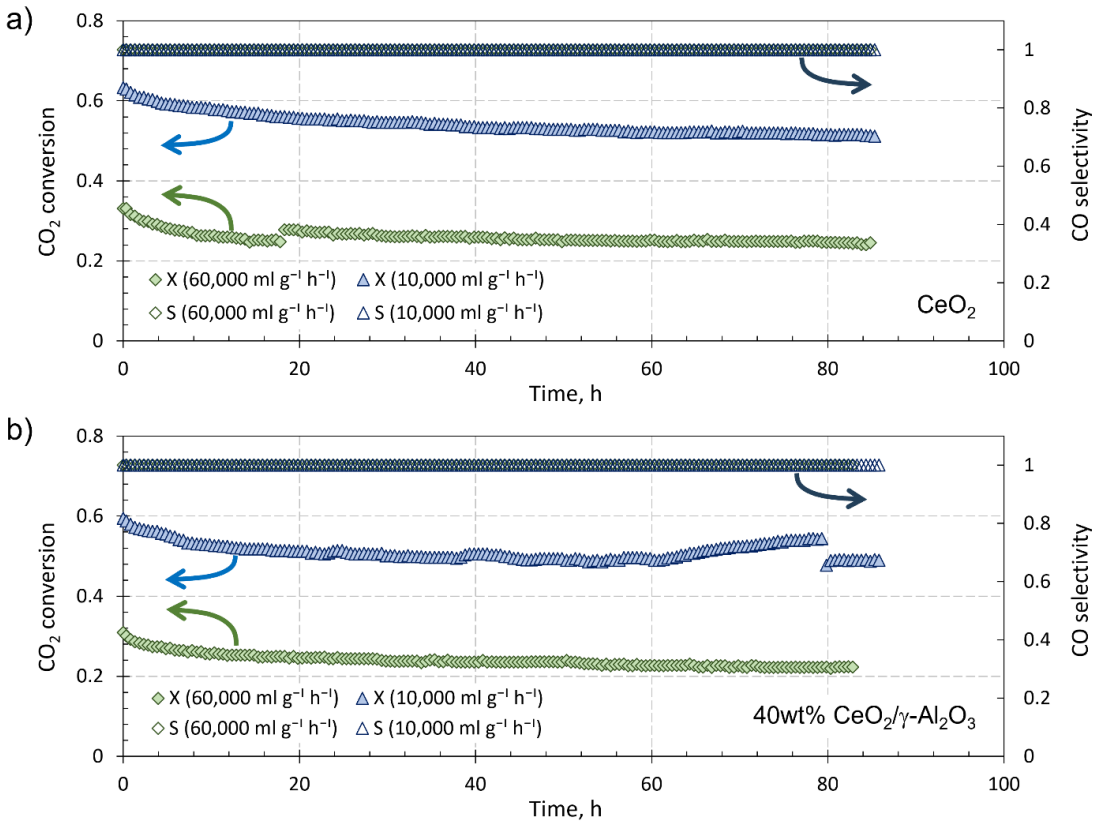

Figure 22. Stability test for CeO_2 (a) and 40wt% CeO_2/γ-Al_2O_3 (b). Parameters: P = 1 bar, H_2/CO_2 = 3 (feed), GHSV = 10,000 mL/(g h) and 60,000 mL/(g h), T = 600 °C..

For the 40wt% CeO_2 catalyst, very similar behavior was observed, both in terms of conversion values and dynamics. Except for the initial loss in conversion during the first 10-20 h, both catalysts were relatively stable, while showing complete selectivity to CO formation. Importantly, the stability behavior of the 40wt% CeO_2 catalyst was very similar to that of the pure CeO_2 catalyst, even though the amount of CeO_2 was significantly (more

than two-fold) lower (**Table 2**). To investigate the reason for the similar performance of the pure CeO_2 and 40wt% CeO_2 catalysts, transient changes in the specific surface area (SSA) and nanoparticle size were investigated via gas adsorption and X-ray diffraction.

4.3. Transient changes in catalyst nanomorphology

In separate stability tests conducted for CeO_2 and 40wt% CeO_2, the reaction was stopped, and the reactor was cooled down to room temperature (under the flow of N_2) at certain times (10, 40, and 80 h), to collect samples for catalyst morphology characterization, subsequently resuming the reaction. The results of catalyst characterization are shown in **Figures 23-25**. **Figure 23** shows the obtained XRD patterns (for γ-Al_2O_3, 40wt% CeO_2, and CeO_2 for samples collected at different times during the stability test.

The observed XRD peaks for CeO_2 confirmed the typical fluorite structure [23]. For 40wt% CeO_2, the same structure was observed, with only 28.9°, 47.3° and 56.9° locations showing clear peaks, with other locations detectable as broad/overlapping peaks. For γ-Al_2O_3, a pattern typical for γ-Al_2O_3 was observed, at/after 10 h, with the initial pattern showing largely amorphous structure. The highest intensity peak located at 67.2° was also observed in the 40wt% CeO_2 sample.

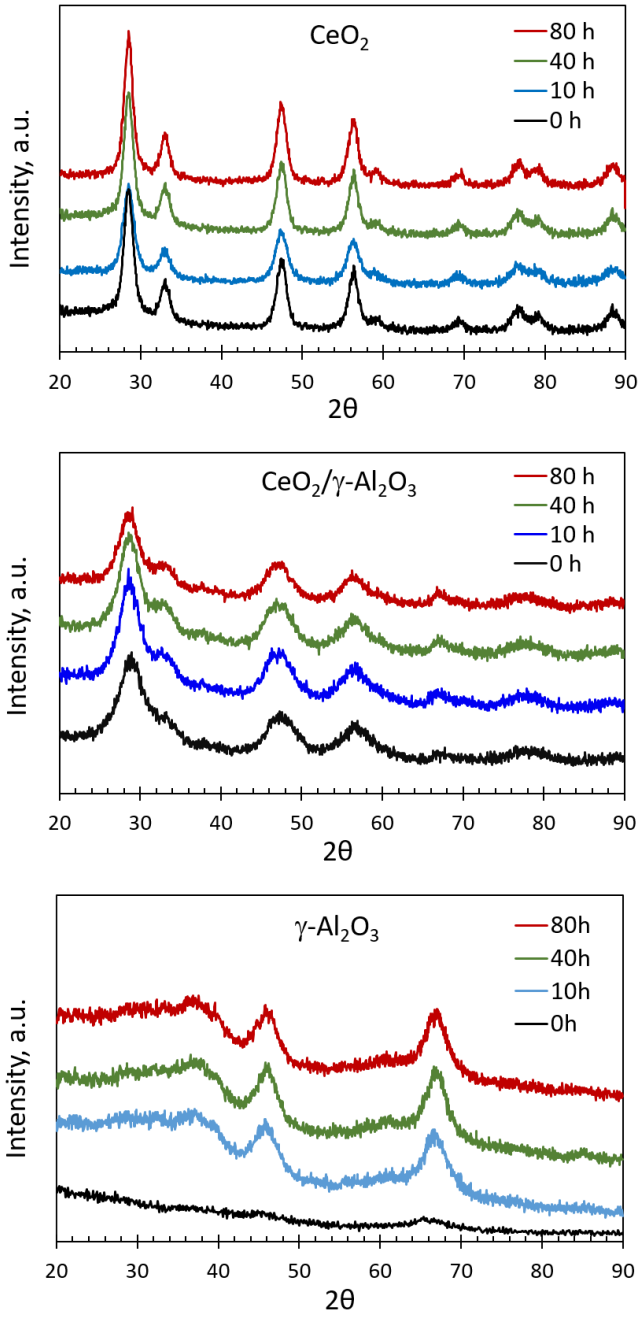

Figure 23. XRD patters of CeO_2 (upper plot), 40wt% CeO_2/γ-Al_2O_3 (middle plot), and γ-Al_2O_3 (lower plot) samples collected from the reactor at different times during the stability test. Parameters for stability test: P = 1 bar, H_2/CO_2 = 3 (feed), GHSV = 20,000 mL/(g h), T = 500 °C.

There are two important observations from the XRD analysis of the samples collected at different times. First, the observed peak broadening for all analyzed samples is indicative of CeO_2 and γ-Al_2O_3 particles approaching the nanoscale (below 20 nm). Second, it can be concluded that CeO_2 nanoparticles are smaller in the 40wt% CeO_2 as compared to pure CeO_2. Detailed analysis of nanoparticle size is discussed later (see **Figure 25** and corresponding discussion). At this point, it is important to emphasize that, first, γ-Al_2O_3-supported CeO_2 preserves the typical fluorite structure of CeO_2 and, second, dispersing CeO_2 on γ-Al_2O_3 results in a smaller γ-Al_2O_3 nanoparticle size. Also, since the peak broadening does not change significantly through the experiment (80 h), it can be concluded that there is no drastic change in nanoparticle size.

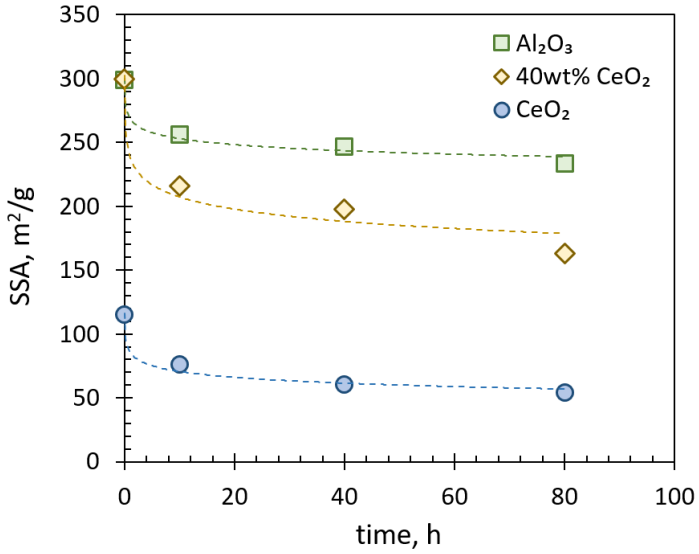

Figure 24. Specific surface area vs. time for CeO_2 (circles), 40% CeO_2/γ-Al_2O_3 (rhombs), and γ-Al_2O_3 (squares). Samples were collected from the reactor during the stability test at different times (see SI for detailed description). Stability test parameters: P = 1 bar, H_2/CO_2 = 3 (feed), GHSV = 20,000 mL/(g h), T = 500 °C.

To further analyze the morphology of the collected samples, specific surface area (SSA) was measured for all collected samples. **Figure 24** presents the SSA data for the CeO_2, 40wt% CeO_2, and γ-Al_2O_3 samples collected at different times during the same stability test. At the start of the experiment, the 40wt% CeO_2 catalyst had SSA of 299.7 m^2/g, which is consistent with the value reported in Table 1. The γ-Al_2O_3 sample had virtually identical SSA of 299.0 m^2/g. For the bulk CeO_2 sample, SSA was significantly lower (115 m^2/g), consistently with a previous publication [23].

While comparing the initial and final SSA values for all three samples, significant reduction in SSA was observed for all samples. However, from the point of view of SSA change dynamics, most of the change occurred during the first 10 h of operation, which can be simply attributed to the low calcination temperature used in catalyst synthesis (275 °C, see *Section 3.1*). After this initial change, further reduction in SSA is relatively minor. Importantly, SSA for the 40wt% CeO_2 catalyst was significantly higher than that for the pure CeO_2 sample (299.7 m^2/g vs. 115 m^2/g), presumably attributed to the high SSA value of the γ-Al_2O_3 support. To deconvolute the contribution of CeO_2 and γ-Al_2O_3 phases to the total SSA value, crystallite sizes were calculated from the XRD data.

Figure 25 presents nanoparticle sizes calculated from the data shown in **Figure 23 and Figure 24**. To calculate the SSA-based nanoparticle size, Eq. (17) was used, with the weight averaged density calculated by Eq. (17a**)** (*x* is the CeO_2 weight fraction, as determined by ICP-OES). It is important to clarify that Eq. (17) assumes perfectly spherical particles completely exposed to gas phase, which is unrealistic as nanoparticles typically deviate from the spherical shape and, even more importantly, tend to agglomerate. Still, such an estimation could be useful for the purpose of comparison. To calculate the XRD-

based nanoparticle size, crystallite size was calculated from the XRD peak broadening using Scherrer equation, Eq. (4). For CeO_2 phase, 28.9°, 47.3° and 56.9° peak locations were used (reporting average values with standard deviations). For γ-Al_2O_3, 45.9° and 67.2° peak locations were used for pure γ-Al_2O_3, while for the 40wt% CeO_2 sample only 67.2° peak was detectable.

$$d(SSA) = \frac{6000}{\rho_P \times SSA} \quad \textbf{(17)}$$

$$\rho_P = (x) \times \rho_{CeO_2} + (1-x)\rho_{\gamma-Al_2O_3} \quad \textbf{(17a)}$$

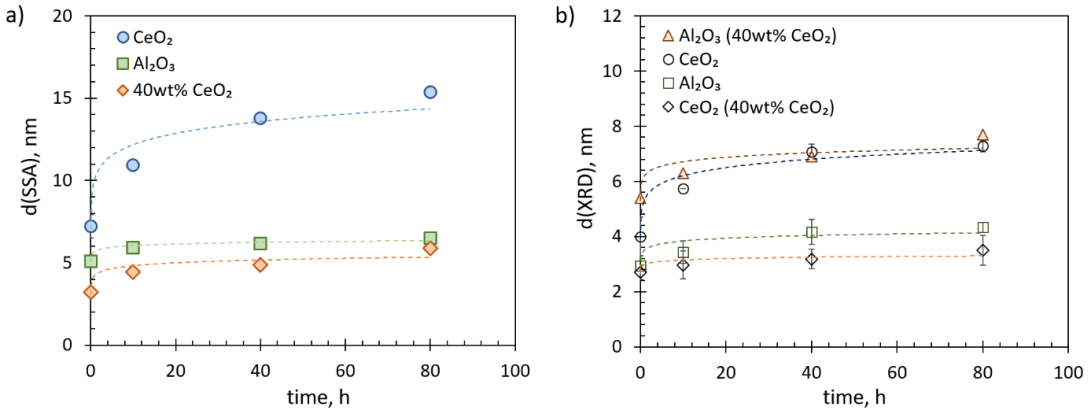

Figure 25. SSA-based nanoparticle size calculated by Eq. (7) for pure CeO_2 (circles), pure γ-Al_2O_3 (squares), and 40wt% CeO_2/γ-Al_2O_3 (rhombs) (a), and XRD-based crystallite size calculated by Eq. (8) for γ-Al_2O_3 in 40wt% CeO_2/γ-Al_2O_3 (triangles), pure CeO_2 (circles), pure γ-Al_2O_3 (squares), and CeO_2 in 40wt% CeO_2/γ-Al_2O_3 (rhombs). For d(XRD), error bars show standard deviation between crystallite sizes calculated at different peak locations.

For pure γ-Al_2O_3, nanoparticle sizes calculated based on SSA and XRD were very similar, namely 6.5 nm and 4.3 nm, respectively (at the end of the experiment). This result points out at a relatively small degree of agglomeration and/or nearly spherical shape of

the γ-Al_2O_3 nanoparticles. It can be concluded that the RME-synthesized γ-Al_2O_3 consists of well-dispersed nanoparticles that do not grow significantly at 500 °C while being exposed to CO_2/H_2 mixture. With respect to pure CeO_2, there was a substantial (ca. two-fold) difference between the SSA- and XRD-based nanoparticle size (15.4 nm vs. 7.3 nm), indicating a significant degree of nanoparticle agglomeration, as previously reported [23].

For the 40wt% CeO_2 catalyst, the XRD-based crystallite size for the γ-Al_2O_3 phase was similar to that of pure γ-Al_2O_3 (7.7 nm vs. 6.5 nm), indicating that introducing the Ce precursor into the RME synthesis procedure does not affect significantly the γ-Al_2O_3 nanoparticle size. With respect to the CeO_2 phase in the 40wt% CeO_2/γ-Al_2O_3 catalyst, the XRD-based crystallite size was notably smaller than that in the pure CeO_2 sample (3.5 nm vs. 15.4 nm). This finding is a key result that explains similar performance of the 40wt% CeO_2/γ-Al_2O_3 and CeO_2 catalysts. It can be concluded that the interaction between CeO_2 and γ-Al_2O_3 phases plays a crucial role in hindering the growth of CeO_2 nanoparticles. Notably, in pure CeO_2 the nanoparticle growth was 113.9% (7.2 nm to 15.4 nm), while in 40wt% CeO_2, the CeO_2 nanoparticle growth was only 29.6% (2.7 nm to 3.5 nm).

Chapter 5: RWGS activity enhancement in $CuCeO_2$ catalyst

5.1 Catalyst composition, crystallinity, and morphology

Figure 26 shows XRD patterns of fresh (calcined) and spent (post-reaction) catalysts. The percentages reported (0, 0.62, 1.17, 5.36, 10.20 and 26.54%) refer to atomic percentages (at%) calculated as Cu/(Ce+Cu) on molar basis as determined by ICP-OES (**Table 3**). Diffraction peaks for fresh catalysts are broad, which is indicative of small nanocrystallite size. Spent catalysts show clear, sharp peaks. The patterns of both fresh and spent catalysts correspond to the CeO_2 fluorite structure (PDF 00-034-0394). All XRD patterns showed no presence of additional crystalline phases of Cu or Cu oxides (CuO or Cu_2O), implying that Cu was predominately incorporated into the CeO_2 lattice by replacing Ce ions. The presence of certain sub-nanometric clusters of Cu or Cu oxides on the surface is also possible, as such clusters will not be detectable by XRD. This observation of a high level of Cu doping is consistent with previously reported literature, e.g., Muzina et al. reported a maximum Cu doping concentration of 12.4 mol% for CeO_2 [50].

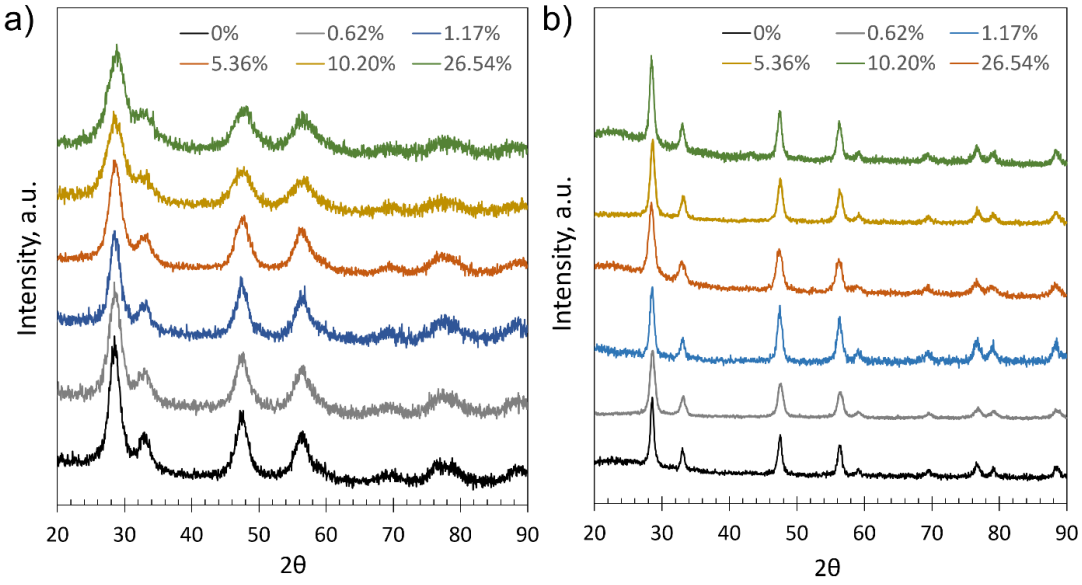

Figure 26. XRD patterns of as prepared, calcined catalysts (a) and of catalysts after 20 h under reaction conditions (b).

Table 3: Cu loading (Cu/(Ce+Cu) at% as determined by ICP-OES), BET-measured specific surface area (SSA), and crystallite size as determined from XRD patterns (D_{XRD}).

Cu loading, at%	**SSA, m^2/g**		**D_{XRD}, nm**	
	fresh	**spent**	**fresh**	**spent**
0	114.4±3.4	15.0±1.6	5.2±0.3	15.1±0.9
0.62	-	-	4.2±0.4	11.2±1.1
1.17	137.8±6.3	21.3±1.8	5.3±0.4	12.0±0.9
5.36	138.5±5.8	31.5±1.1	4.2±0.3	9.8±0.6
10.20	124.0±5.5	12.7±2	3.3±0.3	11.1±1.2
26.54	124.2±6.5	11.3±1.4	3.1±0.1	12.7±0.8

Table 3 shows crystallite sizes calculated from XRD patterns by Scherrer equation. The (111), (220) and (311) (highest intensity) peaks were used to calculate the average crystallite size; deviations reported in Table 1 refer to standard deviations between the three values. The results showed that, for fresh catalysts, the nanocrystallite size decreased as Cu

doping increased, with the crystallite size plateauing after 10.20 at%. Note that Cu^{2+} ionic radius is 0.72 Å, whereas ionic radii of Ce^{4+} and Ce^{3+} are1.01 Å and 1.28 Å, respectively. Thus, substitution of Ce^{4+} and Ce^{3+} by Cu^{2+} may decrease the lattice size, and therefore the crystallite size to certain extent.

The crystallite size of the spent catalyst was observed to increase by approximately 2 to 3 times compared to the fresh catalyst. This increase can be attributed to the occurrence of aggregation at high temperatures when the catalyst interacts with the reactants, leading to a larger particle size. Interestingly, the crystallite size of spent catalysts did not follow the same trend as that of fresh catalysts. The crystallite size is influenced by two factors: substitution of a larger ionic radius ion (Ce^{4+} = 1.01 Å) with a smaller one (Cu^{2+} = 0.72 Å) which decreased the overall crystallite size, and the generation of oxygen vacancies due to Cu doping which can have an opposite effect (lattice expansion) [51]. Consequently, these two factors may have an impact on the crystallite size of the spent catalysts leading to a more complicated relationship between the Cu doping level and the nanocrystallite size. However, as lattice size is not necessarily directly correlated with nanocrystallite size, it has to emphasized that other factors can potentially affect the observed differences.

BET specific surface area (SSA) measured by N_2 adsorption showed that SSA is higher at lower Cu doping concentrations for fresh catalysts but decreases with doping concentration for 10.20 and 26.54 at%. The spent catalyst exhibits a substantial reduction in SSA ranging, from 77.6-98.7% under the reaction conditions. It is noteworthy that all catalysts were calcined at lower temperature (275 °C) before the reaction tests, which were conducted at 300-600 °C. This lower calcination temperature contributed to a significant degree of agglomeration, as seen in XRD results, leading to a lower SSA value.

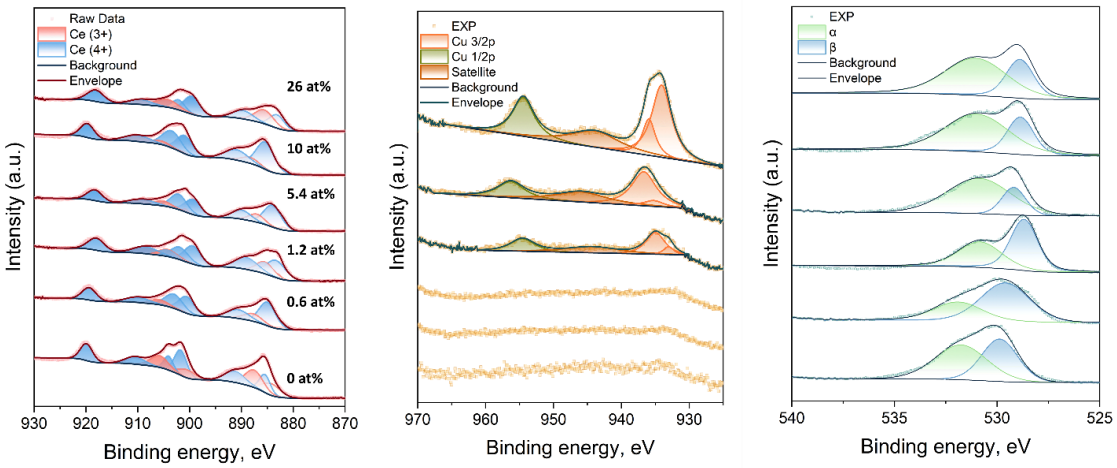

Figure 27. XPS spectra of fresh (calcined) catalysts showing Ce 3d, Cu 2p, and O1s regions for pure CeO_2 (0 at%) and Cu-doped CeO_2 (0.62-26.54 at%).

Surface elemental composition and chemical states were evaluated through XPS (**Figure 27**). The Ce 3d subshell consists of 5 orbitals with 2 different spin states ($3d_{5/2}$ and $3d_{3/2}$). It is generally well accepted that CeO_2 has 10 well fitted peaks with the $3d_{5/2}$ and $3d_{3/2}$ doublet peaks having a 3:2 peak area ratio [52]. The following peak fitting criteria were used to get 10 well fitted peaks for all samples: u_o, u, u', u'', u''', v_o, v, v', v'', v''' (u represents peaks associated with the $3d_{5/2}$ spin state, while v represents peaks associated with the $3d_{3/2}$ spin state). Concentration of Ce^{3+} and Ce^{4+} states can be summarized as follows (with **Eq. (20)** representing the fraction of Ce^{3+} ions) [53]:

$$Ce^{3+} = u_0 + u' + v_0 + v' \tag{18}$$

$$Ce^{4+} = u + u'' + u''' + v + v'' + v''' \tag{19}$$

$$Ce^{3+} = \frac{Ce^{3+}}{Ce^{3+} + Ce^{4+}} \tag{20}$$

Ce^{3+} and Ce^{4+} represent the sum of the areas of the peaks associated with each oxidation state. **Figure 28** shows the Ce^{3+} fraction plotted against the Cu doping level. Interestingly,

the concentration of Ce^{3+} decreases drastically upon incorporation of Cu, with an additional decrease as the Cu doping level increases (except for the highest Cu loading). This observation suggests that Cu substitutes Ce^{3+} sites on/near the surface (XPS only provides information about a few subsurface atomic layers, although for nanoparticles of less than 5 nm it will be most of the atoms).

It is well known that higher concentrations of Ce^{3+} can results in higher concentrations of oxygen vacancies that are known to form around the Ce^{3+} ion [54]. Therefore, reduction in Ce^{3+} concentration reduces the concentration of oxygen vacancies. On the other hand, additional oxygen vacancy sites can form around Cu^{2+} ions, increasing the concentration of oxygen vacancies by Cu doping. Wang et al. conducted a combined density functional theory (DFT) and experimental study for Cu-doped CeO_2 and concluded that Ce substitution by Cu can form up to 3 oxygen vacancy sites surrounding each Cu^{2+} ion [55]. As a result, the substitution of Ce^{3+} with Cu^{2+} can significantly increase the concentration of oxygen vacancy sites, thus enhancing the chemisorption capability of CO_2. It is interesting that at 26.54 at% Ce^{3+} concentration increases substantially, although still being significantly lower than that for pure CeO_2.

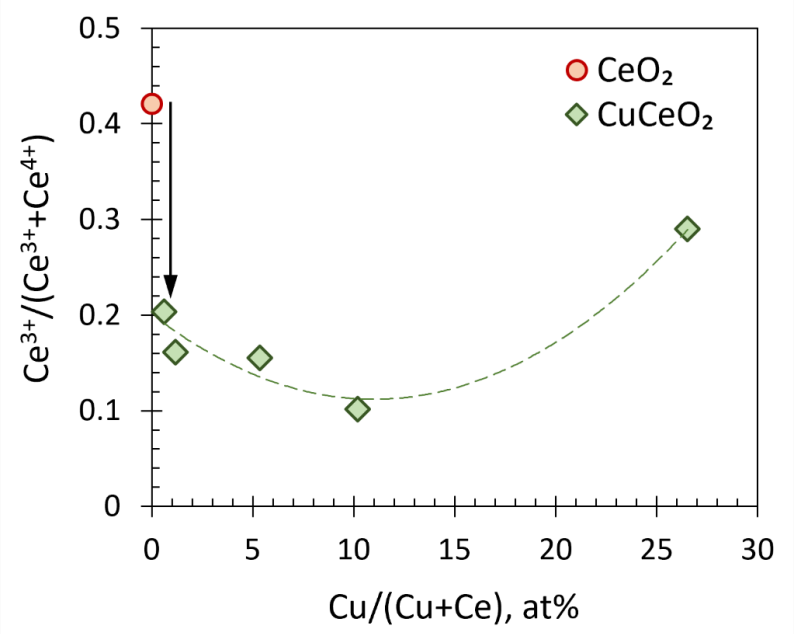

Figure 28. XPS-measured $Ce^{3+}/(Ce^{3+} + Ce^{4+})$ chemical state ratio vs. Cu/(Cu+Ce) atomic ratio as determined by ICP-OES.

XPS spectra of the Cu 2p core level (middle panel in **Figure 27**) were only detectable for relatively high Cu doping levels (5.4-26.5 at%). Cu 2p spectra were deconvoluted into 4 distinct peaks which are consistent with two Cu $2p_{3/2}$ peaks (935.3 and 936.2 eV), one Cu $2p_{1/2}$ peak (956.2 eV) and a satellite peak (945.7 eV). The presence of the satellite peak alongside higher binding energies for Cu $2p_{1/2}$ suggests that Cu^{2+} was present in the sample [56]. Peaks located between 933-936 eV can be ascribed to Cu^{+} and Cu^{0} states. However, binding energies of Cu^{+} and Cu^{0} are very similar and they are difficult to be distinguished on the basis of their Cu $2p_{3/2}$ binding energies alone [57], and further analysis might be required to determine the exact chemical state of Cu [58]. To sum up, the analysis of the Cu 2p core level confirmed the presence of Cu^{2+} in the sample, which is consistent with the analysis of the Ce 3d data indicating substitution of Ce^{3+} with Cu^{2+}.

O1s spectra (right panel in **Figure 27**) was deconvoluted into two separate peaks (except for pure CeO_2 and 0.62 at% Cu loading). The first peak located at 528-529 eV (denoted as O_β) is typically associated with lattice oxygen, while the second peak located at 530-531 eV (denoted as O_α) is associated with either surface oxygen or oxygen defect [59]. The presence of oxygen defect sites is typically associated with improved oxygen mobility that can in turn enhance oxygen vacancy formation.

5.2 CO_2 adsorption strength analysis

Combined CO_2 TPD-FTIR analysis of pure CeO_2 and 10.20 at% Cu-doped CeO_2 (both unreduced and reduced samples) are shown in **Figure 29**. As expected, the evolution of CO_2 throughout the experiment matched the evolution of the TCD signal, also confirming the validity of the experiment. For unreduced CeO_2(Figure 4a), two peaks are observed in the temperature-programmed desorption (TPD) curve, occurring at 96 °C and 147 °C. In the case of unreduced 10.20 at% (Figure 4c), three peaks are visible at 95 °C, 233 °C, and 416 °C. Upon reduction, both CeO_2 and 10.20 at% CeO_2 exhibit a similar shape in the TPD curve. Both samples display a low-temperature peak around 80-84 °C. However, there is a shift in the peak location of the second peak for 10.20 at% as compared to. CeO_2. Further discussion on this topic will be provided later. In both reduced and unreduced CeO_2 and 10.20 at% catalysts, a weak CO signal was observed. This suggests the possible occurrence of CO_2 dissociation to CO at higher temperatures. Notably, in the reduced samples, stronger CO signals were detected compared to the unreduced samples. This could indicate that the reduction process enhances the dissociation of CO_2 and leads to a higher production of CO.

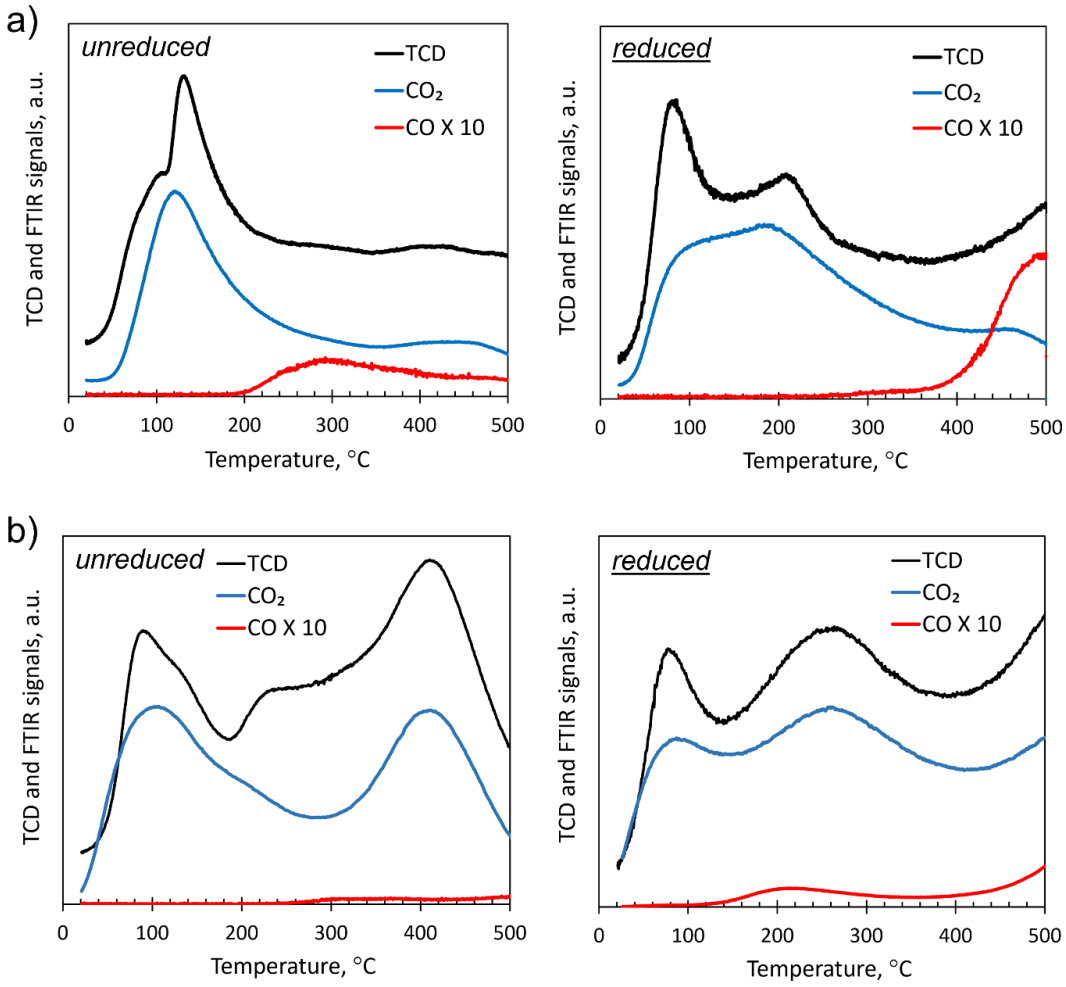

Figure 29. CO_2 TPD-FTIR analysis of the fresh (calcined) samples of CeO_2 (a) and 10.20 at% Cu-doped CeO_2 (b). Evolution of CO and CO_2 in the off-gas was detected by continuous flow FTIR (shown as FTIR signals). For reduced samples (right panel), the reduction was conducted at 400 °C using 10% H_2/Ar (30 mL/min).

Figure 30 presents the CO_2 TPD results for unreduced and reduced catalysts. Two distinct peaks (denoted as α and β) are observed at relatively low temperatures, as well as a high-temperature peak denoted with γ. For unreduced samples, the α-peak was located at similar temperature (ca. 90-100 °C) for all doping concentrations (including pure CeO_2). The β-peak (which was not clearly differentiable for 26.54 at%) was slightly shifted to a

higher temperature (from ca. 150 °C to ca. 170 °C) for intermediate Cu doping levels. The γ-peak was located at ca. 410-420 °C for all samples.

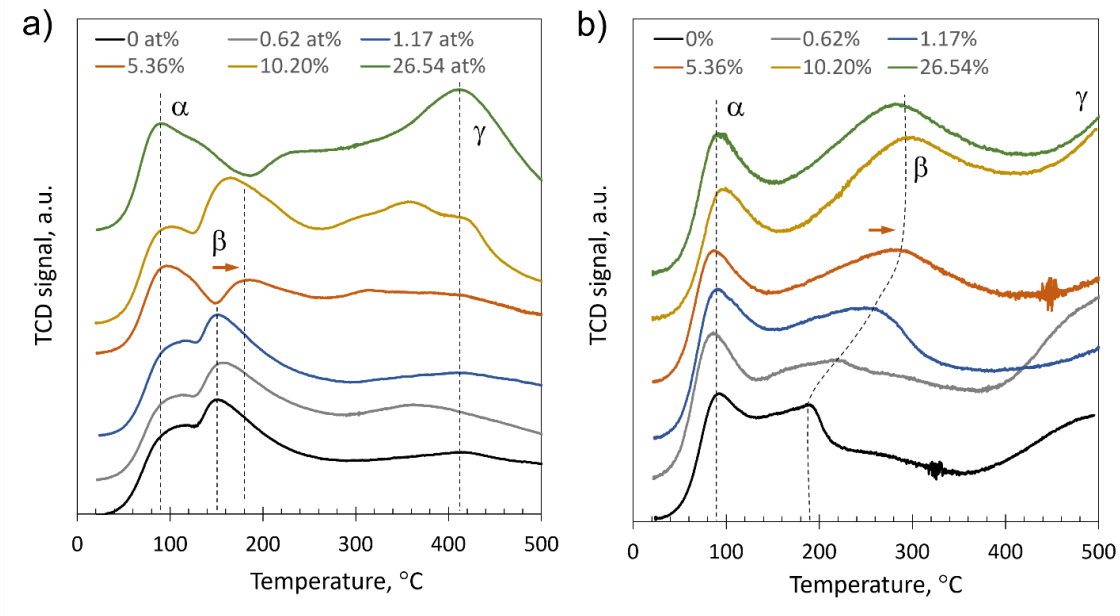

Figure 30. CO_2 TPD profiles obtained for unreduced (fresh, after calcination) samples (a) and samples after reduction at 400 °C (b).

For reduced samples, the α-peak became clearer, and its location remained unchanged. On the contrary, the β-peak was clearly shifted to significantly higher temperatures for increased Cu loadings (from ca. 190 °C to ca. 300 °C at high Cu doping levels). The γ-peak was consistently shifted for all samples so that the location of its maximum was at temperatures higher than 500 °C.

The three observed desorption peaks are clearly associated with three different adsorption sites/configurations for CO_2, corresponding to weak, moderate, and strong CO_2 adsorption strength, respectively. The α-peak could be associated with bicarbonate desorption owning to its weak interaction with the surface. On the other hand, the β- and

γ-peaks could be associated with monodendate or bidendate desorption, as these species exhibit a higher binding strength to the surface [60].

Furthermore, the activation energy of desorption ($E_{a,des}$) was calculated from the obtained TPD profiles by Polanyi-Wigner equation, Eq. (5). **Figure 31** shows the obtained values for α- and β-peaks plotted versus Cu loading. For the α-peak, $E_{a,des}$ values were very similar for all samples (both unreduced and reduced), except for 10.20 at% from which a substantial decrease was observed for the reduced sample. For the β-peak, there was a relatively small increase for unreduced samples (not shown for 26.54 at% because it was difficult to detect). However, for reduced samples it was a clearly observable increase in $E_{a,des}$ values for small Cu doping concentrations, achieving a certain plateau at 5.36-26.54 at%. On overall, there is a drastic increase in $E_{a,des}$ for the reduced catalyst from 145 kJ/mol at 0 at% to 173 kJ/mol at 26.54 at%.

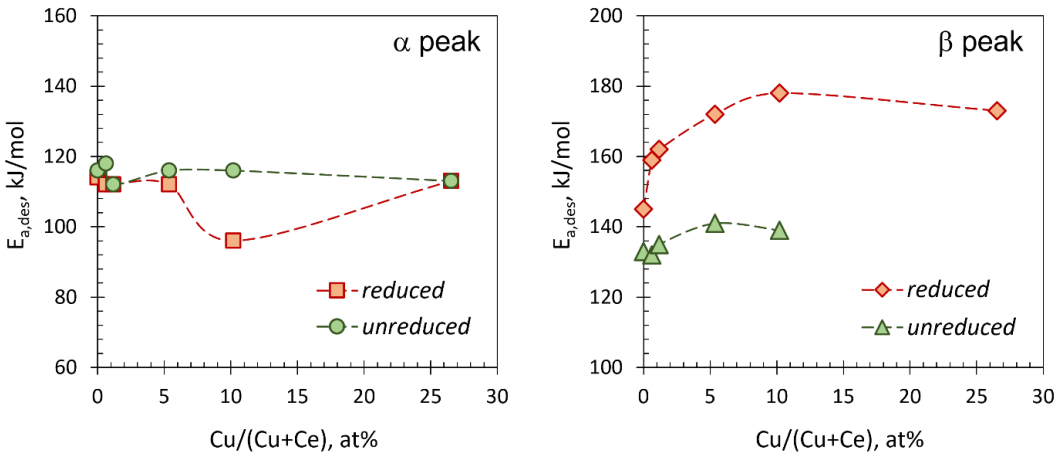

Figure 31. Activation energy of desorption ($E_{a,des}$) vs. Cu loading (Cu/(Cu+Ce)) for α-peak (left panel) β-peak (right panel); α- and β-peaks correspond to CO_2 TPD peaks presented in Fig. 5.

The increase in the activation energy of CO_2 desorption for the β-peak, indicates that this particular adsorption site/configuration peak could be related to surface oxygen vacancies formed due to Cu incorporation. These sites could be responsible for stronger CO_2 adsorption. Note that the XPS results pointed out at the possibility of the increase in the oxygen vacancy concentration due to the Cu^{2+} substitution of Ce^{3+} (**Figure 28**).

5.3 Catalytic performance evaluation

Catalyst performance was evaluated in terms of CO_2 conversion and CO selectivity via reaction tests conducted in the range of temperatures and space velocities (**Figure 32**). All catalysts were reduced in pure H_2 before switching to H_2/CO_2 feed mixture *(see Section 3.3 for details).*

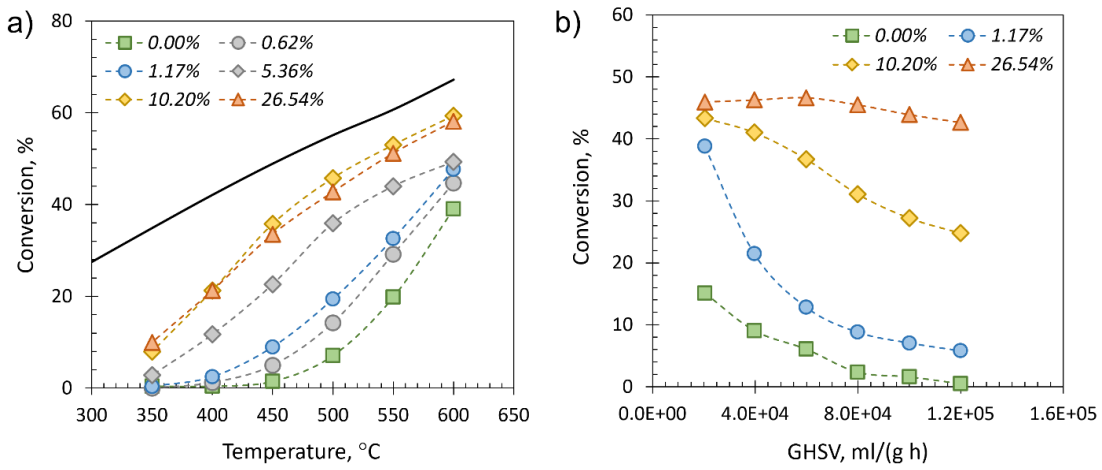

Figure 32. Catalytic performance evaluation as a function of temperature (a) and space velocity (b). Solid black line in (a) represents RWGS equilibrium. Parameters: P = 3 bar, H_2/CO_2 = 3, GHSV = 60,000 mL/(g h) (a) and T = 500 °C (b).

Figure 32a shows CO_2 conversion as a function of temperature. All samples were 100% selective to CO generation (no CH_4 formation was observed in the entire temperature range). CO_2 conversion was only detectable at 400 °C for Cu doping concentration of 0-

1.13 at% (0 at% represents pure CeO_2). For pure CeO_2 the maximum conversion was ca. 40% at 600 °C. The Cu doping concentrations of 1.13 and 5.2 at% yielded conversion values of 47% and 49%, respectively at 600 °C. For 10.2 at% and 26.54 at%, there was a notable increase in performance, detectable at lower temperatures as well. At 400 °C, CO_2 conversion for 10.2 at% and 26.54 at% exhibited a remarkable two-fold improvement compared to CeO_2, reaching ca. 20%, while at higher temperatures conversion values were close to equilibrium (ca. 60% at 600 °C). Interestingly, 10.2 at% and 26.54 at% had quite similar catalytic performance, indicating that there is a limit to Cu doping beyond which further addition of Cu does not significantly change the catalytic performance.

To further evaluate the catalytic performance, reaction tests were conducted for selected samples at a fixed temperature of 500 °C and in a range of space velocities (20,000 ml/(g h)-120,000 ml/(g h)) (**Figure 32b**). Similarly to the reaction tests in the range of temperature, CO selectivity remained 100% for all catalysts tested and in the entire range of space velocities. As expected, all catalysts performed significantly better at lower GHSV, due to the increased residence time. Consistently with previous tests (**Figure 32a**), pure CeO_2 showed relatively poor performance, with the conversion reaching zero at 120,000 ml/(g h). Cu-doped catalysts performed significantly better at 20,000 ml/(g h), with, showing conversion in the range of 38-45%. The conversion profile for 1.4 at% drops repeatedly and plateaus as GHSV increases. In contrast, the drop in conversion at higher doping concentrations (10.2 and 26.54 at%) was less pronounced, in particular for 26.54 at%. These observations indicate that catalysts with higher Cu loadings are significantly more active.

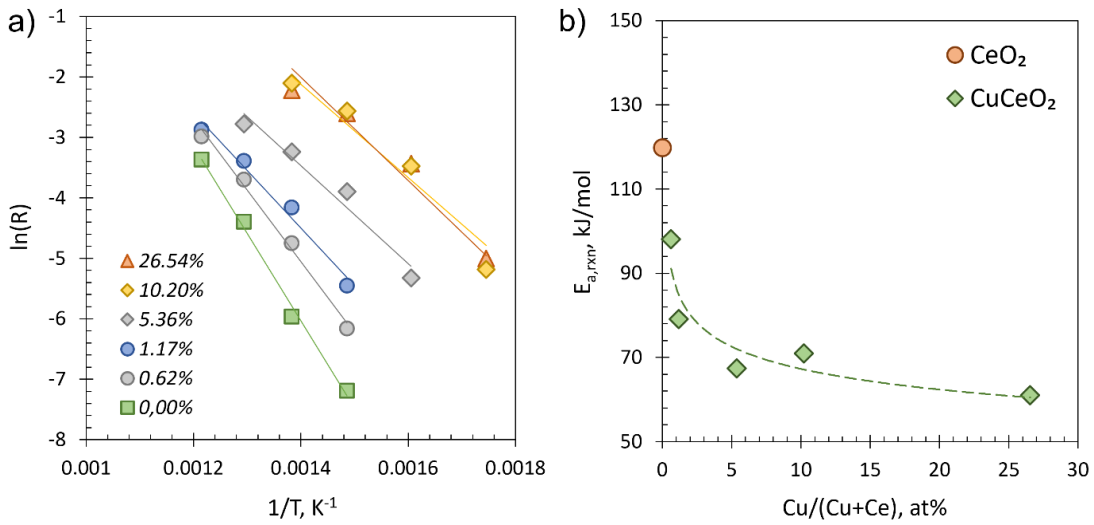

Figure 33. Arrhenius plots (a) and corresponding reaction activation energies ($E_{a,rxn}$) vs. Cu loading (b).

Arrhenius plots shown in **Figure 33a** were obtained in a separate set of reactions tests. Temperature was held below 500 °C and GHSV was adjusted to ensure that CO_2 conversion does not exceed 20%. CO generation rates were calculated from **Eq. (21)** and activation energy estimation was done using **Eq. (22).**

$$R_{CO} = \frac{F_{CO_{2,f}} X_{CO_2}}{W_C} \tag{21}$$

$$\ln(R_{CO}) = \ln(A) - \frac{E_{a,rxn}}{R_g T} \tag{22}$$

Figure 33b shows the estimated values plotted vs. Cu loading. Notably, $E_{a,rxn}$ values exhibited a significant decrease from 119 kJ/mol for pure CeO_2 to 60 kJ/mol for 26.54 at% Cu loading. Interestingly, as the Cu doping concentration increases, $E_{a,rxn}$ values demonstrate a highly non-linear decreasing trend with a sharp initial decrease followed by a moderate decrease at higher Cu loadings. The reduction of $E_{a,rxn}$ in Cu-doped samples

can be attributed to generation of additional oxygen vacancies that facilitate CO_2 adsorption and activation.

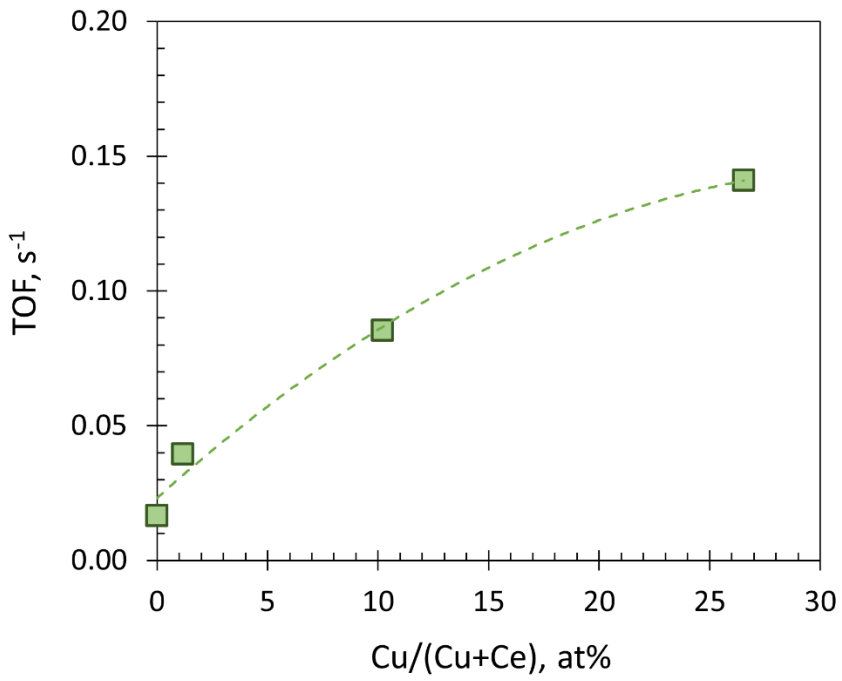

Figure 34. Turnover frequency (TOF) vs. Cu loading. Parameters: P = 3 bar, H_2/CO_2 = 3, T = 500 °C.

Figure 34 shows TOF values calculated for selected samples using Eqs. (9-11). There is a notable increase in TOF from 0.02 to 0.15 s^{-1} as the Cu doping concentration increases from 0 to 26.54 at%. This increase in TOF is consistent with the lower values of reaction activation energies obtained for Cu-doped samples.

5.4 Catalyst stability investigation

A stability test was conducted for the 1.17 at% Cu-loading catalyst (in a quartz tube and atmospheric pressure, see *Section 3.3* for details). The results are shown in **Figure 35**, showing the time evolution of CO_2 conversion and CO selectivity, as well as carbon

balance. Space velocity was gradually increased in a stepwise manner throughout the experiment, and then returned to its initial value towards the end of the experiment, also increasing temperature to 700 °C, and then 800 °C.

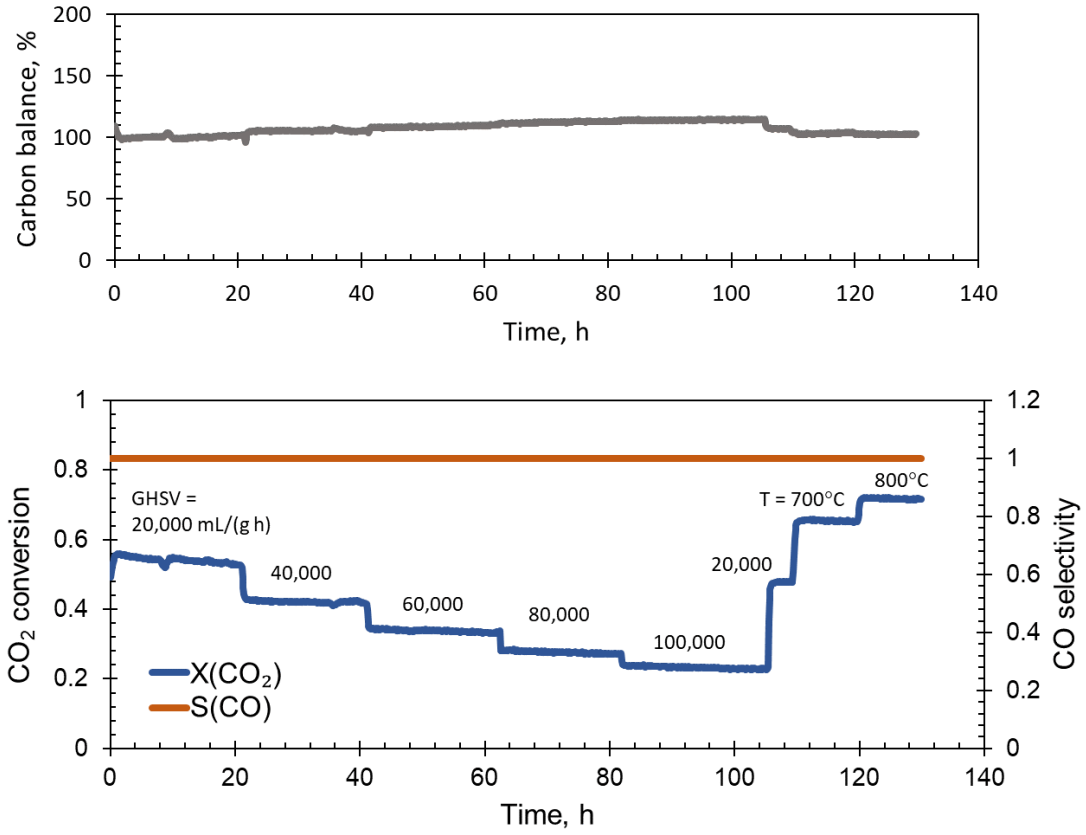

Figure 35. Stability test for the 1.17 at% Cu loading catalyst, showing carbon balance (upper plot) and CO_2 conversion and CO selectivity (lower plot) as a function of time. Space velocity was increased stepwise from 20,000 to 100,000 ml/(g h), and then to 20,000 ml/(g h). Parameters: P = 1 bar, H_2/CO_2 = 3, T = 600 °C (except for last two steps where the temperature was increased to 700 °C, and then to 800 °C).

The initial conversion at 20,000 ml/(g h) was ca. 55%, gradually decreasing for higher GHSV values (as expected). At 60,000 ml/(g h) the conversion was 35%, while 47% was achieved in the reaction test reported in **Figure 32a** at the same temperature and space

velocity. This difference may be attributed to the prolonged exposure of the catalyst under reaction conditions. As GHSV increased, the conversion gradually declined (lower residence time) to 0.23 at 100,000 ml/(g h). Towards the end of the stability test, GHSV was increased to 20,000 ml/(g h) again and the conversion was 0.47. The catalyst demonstrated excellent performance throughout the 110 h test, exhibiting only a slight decrease in conversion. Furthermore, the superior performance was further emphasized when the temperature was elevated to 800 °C, resulting in a conversion value of approximately 0.73, which is close to equilibrium conversion. These results show that the catalyst performance only had minimal drop in performance over 110 h on stream after which still achieving equilibrium conversion when the temperature was increased to 800 °C.

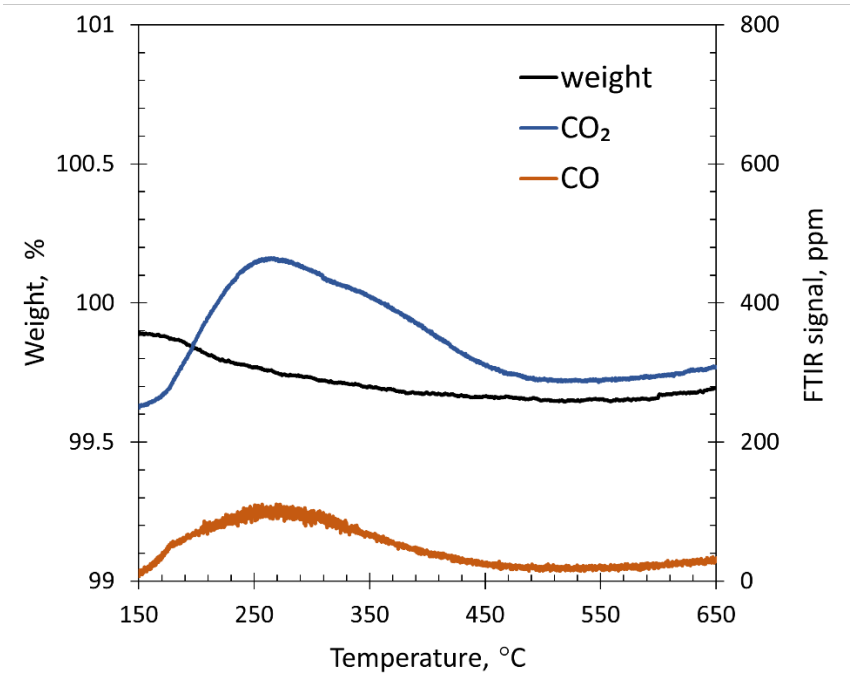

Figure 36. TGA-FTIR analysis of the spent 1.4 at% Cu loading catalyst after stability test at T = 500 °C.

To investigate the extent of carbon deposition on the catalyst, TGA-FTIR analysis was conducted on the spent catalyst recovered from the stability test (**Figure 36**). The sample had a weight loss of around 0.3% which was associated with broad peaks of CO_2 and CO center at 250-350 °C. Given that the slight weight loss observed along with gas peaks linked to carbonaceous species, it can be inferred that a small quantity carbon had formed on the catalyst surface. Another possible explanation for the weight loss could be due to physically adsorbed CO_2 and CO that is being desorbed. This may also result in CO and CO_2 signal seen at lower temperature. The amount of weight loss and carbon species detected was negligible and confirms that the degree of coking was negligible and did not affect the catalyst's performance during the stability test.

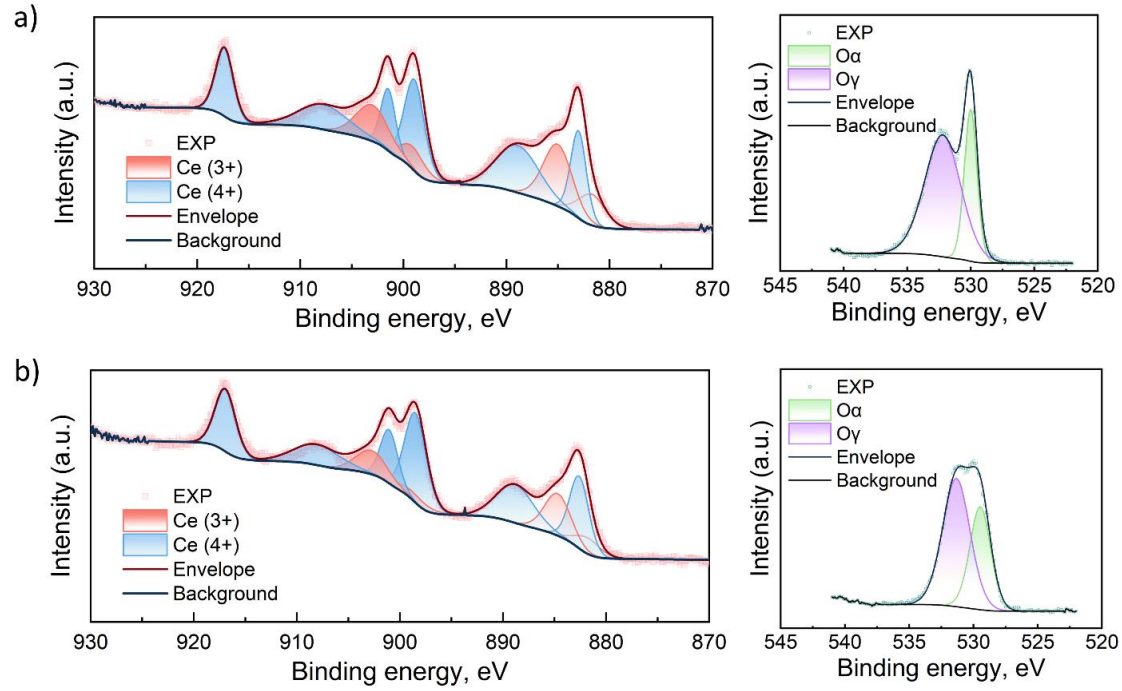

Figure 37. Ce 3d and O1s XPS spectra of spent (post-reaction) pure CeO_2 (a) and spent (post-reaction) 10.20 at% Cu loading catalyst (b).

To get further insights, XPS analysis was conducted on spent catalysts recovered from reaction test **(Figure 32a)**. **Figure 37** shows the XPS spectra of spent pure CeO_2 and 10.20 at% catalysts. The chemical state was investigated by deconvoluting the Ce 3d spectra and calculating the concentration of Ce^{3+} ratio (as explained before in Section 3.1). **Table 4** shows that the concentration of Ce^{3+} increased for the spent 10.20 at% catalyst, whereas it decreased slightly for the spent pure CeO_2 as compared to the respective fresh catalysts. The two-fold increase in Ce^{3+} concentration for 10.20 at% can be explained due to reduction. During reduction, the formation of oxygen vacancies will release two electrons. As a result, the Ce^{4+} converts to Ce^{3+} to ensure electric neutrality which is reflected in the XPS results [61]. However, the same trend is not observed for pure CeO_2. This observation suggests that the CeO_2 could not be reduced further than what was observed in the fresh catalyst.

Table 4. $Ce^{3+}/(Ce^{3+}+Ce^{4+})$ and O_α/O_β ratio of fresh and spent catalysts.

Cu/(Ce +Cu), at%	$Ce^{3+}/(Ce^{3+}+Ce^{4+})$, at%		O_α/O_β	
	fresh	*spent*	*fresh*	*spent*
0	42	38	1.18	2.26
10.2	10	24	2.42	1.65

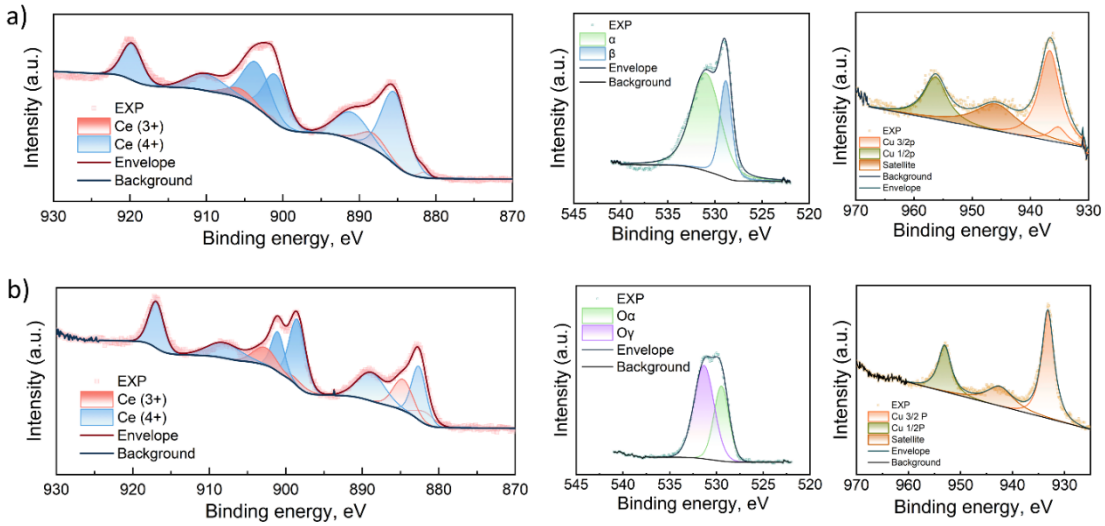

Figure 38. Ce 3d, O1s, and Cu 2p XPS spectra of fresh (calcined) (a) and spent (post-reaction) (b) 10.20 at% Cu loading catalysts.

O1s spectra for the fresh and spent 10.20 at% catalyst are shown in **Figure 38.** Two chemical states were detected for O1s spectra, O_β, which is attributed to lattice oxygen, and O_α,which is assigned to surface oxygen. The position of the O_α and O_β peaks did not change significantly for the fresh and spent catalysts. To examine the differences in the fresh and spent catalysts, the ratio of the area of O_α/O_β were compared. As shown in **Table 4**, O_α/O_β of spent 10.2 at% catalyst decreases by a factor of 1.5. This is because oxygen vacancies can be produced from the surface oxygen (O_α) during reduction by H_2 which results in a decrease in O_α/O_β observed in spent 10.20 at%. On the contrary, the O_α/O_β of 0 at% catalyst increased from 1.18 to 2.26. The O1s results, in conjunction with the Ce 3d findings, provide additional confirmation that $CuCeO_2$ can produce more oxygen vacancies during the reaction as compared to CeO_2. This emphasizes the superior performance of the catalyst, as the increased oxygen vacancies in Cu-doped catalysts account for its enhanced catalytic activity.

5.5 Correlating catalyst activity with adsorption strength

Correlating catalyst activity with adsorption strength is helpful in understating and improving the performance of the catalyst. Specifically, the activation energy of desorption (E_{des}), derived from TPD, and the activation energy of reaction (E_{des}), derived from Arrhenius plot, exhibit noticeable trends with atomic ratio of Cu-doped catalysts **(Figure 39).** E_{des} increases as atomic ratio increases due to increased CO_2 adsorption strength at higher doping concentration and E_{rxn} decreases as atomic ratio increases.

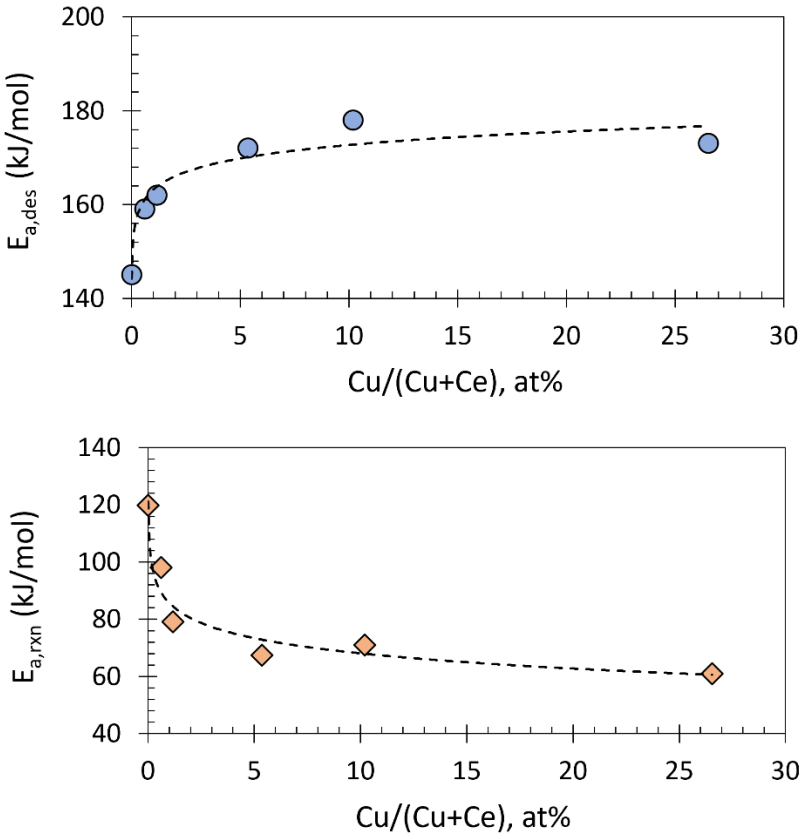

Figure 39. Activation energy of desorption corresponding to β-peak (upper plot) and reaction activation energy (lower pot) vs. Cu loading.

Figure 40 compares $E_{a,des}$ vs $E_{a,rxn}$ where a linear trend is observed. The linear relationship highlights the crucial role of CO_2 adsorption in the reverse water gas shift

reaction. The enhanced adsorption strength of $CuCeO_2$ catalyst can be attributed to increased oxygen vacancies due to Cu^{2+} substitution in CeO_2. The linear trend seen in **Figure 40** shows that the adsorption strength of CO_2 plays a vital role in achieving a lower activation energy. It suggests that the CO_2 adsorption and activation are key contributors to lowering the activation energy of reaction. As a result, the increased CO_2 adsorption strength leads to a lower activation energy of reaction which contributes to the superior performance of the $CuCeO_2$ catalyst. The linear relationship further signifies that $E_{a,des}$ can serve as a useful indicator for evaluating and predicting the catalyst's performance, which facilitates catalyst optimization. This is further emphasized in **Figure 40** which shows the TOF increases as the $E_{a,des}$ increases. The enhanced adsorption strength allows for easier desorption of CO_2, creating more vacant surface sites for new reactant molecules. This means the active sites would be able to convert more reactant molecules, thus increasing the TOF which leads to a superior catalytic performance.

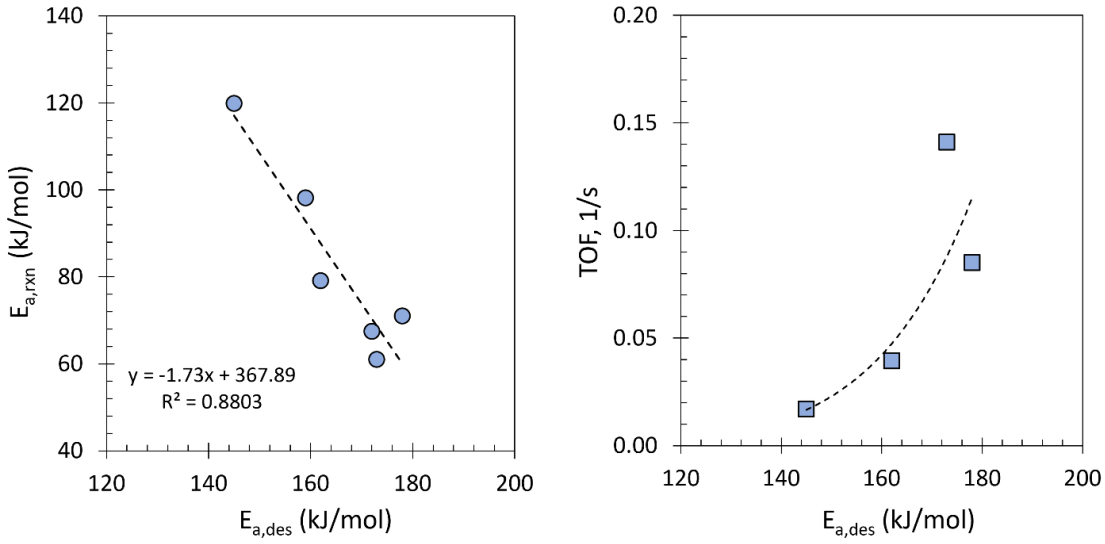

Figure 40. Reaction activation energy ($E_{a,rxn}$) and turnover frequency (TOF) as a function of the activation energy of desorption ($E_{a,des}$) associated with β-peak.

Chapter 6: Conclusion and future work

6.1 Conclusion

The successful investigation of thermocatalytic conversion involved studying the catalytic activity of $CeO_2/\gamma\text{-}Al_2O_3$ and $CuCeO_2$ catalyst. For $CeO_2/\gamma\text{-}Al_2O_3$, the relationship between the particle growth in CeO_2 and $\gamma\text{-}Al_2O_3$ was evaluated for RWGS, while in $CuCeO_2$ the effect to copper doping was explored for the RWGS

A series of high surface area $CeO_2/\gamma\text{-}Al_2O_3$ catalysts were synthesized via the reverse microemulsion method and evaluated for reverse water gas shift for the first time, to the best of authors' knowledge. Reaction tests, including scans over the range of temperature and space velocity and stability test, have shown that the catalyst are completely selective to CO generation and can provide nearly equilibrium CO_2 conversion at relatively low space velocities and elevated temperature (600 °C and 8,000 mL/(g h)). No evidence of significant coke formation was obtained.

As compared to bulk CeO_2, CeO_2 nanoparticle growth in the $CeO_2/\gamma\text{-}Al_2O_3$ catalyst was hindered significantly, resulting in the catalytic performance similar to that of bulk CeO_2. Dispersion of CeO_2 over a $\gamma\text{-}Al_2O_3$ support via the reverse microemulsion methods results in significantly smaller initial CeO_2 nanoparticle size, as well as in hindering the CeO_2 nanoparticle growth and agglomeration. This reduction in the initial nanoparticle size, nanoparticle growth rate, and degree of sintering/agglomeration allows for the enhanced catalytic performance, while using reduced amount of the active phase.

$CuCeO_2$ catalysts with varying Cu doping concentrations were successfully synthesized using the reverse microemulsion method and evaluated for the reverse water gas shift

reaction. XRD showed no separate phase of copper and copper oxides suggesting successful doping into the lattice. Reaction test conducted over a range of temperature and space velocity demonstrated complete selectivity to CO, with the catalysts' activity increasing as the doping concentration increasing. Moreover, stability tests revealed the catalyst was completely stable throughout the test without any significant evidence of coke formation.

The incorporation of Cu^{2+} into the CeO_2 lattice resulted in an increased oxygen vacancy formation on the catalyst surface, thereby increasing the concentration of active sites. Additionally, the observed linear trend between $E_{a,des}$ and $E_{a,rxn}$ suggests that the CO_2 adsorption and activation plays a crucial role in reducing the activation energy of the overall reaction. In addition, the enhanced adsorption strength heightened the availability of vacant active sites, which contributed to superior catalyst performance. As a result, coper doping induced active sites on the surface of the catalyst, resulted in superior CO_2 adsorption strength consequently contributing to the superior performance of the $CuCeO_2$ catalyst.

The interesting thing about this study is it shows how CeO_2 exhibits great versatility as a catalyst in the reverse water gas shift (RWGS) reaction for several reasons. Firstly, CeO_2 has unique redox and oxygen storage properties making it easier to form oxygen vacancies. Furthermore, CeO_2 structure can be modified through metal doping which enhances the catalytic activity of CeO_2 by introducing additional active sites as seen in $CuCeO_2$ experiments. Finally, CeO_2 interacts well with support materials which helps improves the dispersion of the catalyst and strengthens the long term stability performance. Overall, these characteristics make CeO_2 a highly promising catalyst for the RWGS reaction,

especially in harsher conditions where catalyst performance and stability are vital. Its versatility, modified structure through doping, and compatibility with support materials make CeO_2 an excellent candidate for catalytic applications in various industrial settings.

6.2 Future work

In future work, it would be valuable to examine the performance of CeO_2 catalyst with different doping metals such as Fe or Ni and compare the catalytic activity with $CuCeO_2$. Fe has proven to be a good catalyst for RWGS reaction and thus may produce similar results to this thesis. Ni, on the other hand, is known to be more selective to methane, however if it is successfully doped into the CeO_2 lattice it may produce different results and making it more suitable as a RWGS catalyst. This comparison will provide further valuable insight on the effects of doping and help guide what catalyst is more ideal for RWGS reaction.

In addition, the RME process is a chemical-intensive synthesis process and may have some challenges for industrial application. . Developing a synthesis method with reduced chemical requirements while retaining the desired properties of the catalyst, such as high surface area and doping properties, would be crucial for scaling up the production process. A new synthesis method for $CuCeO_2$ that reduces the chemical consumption would be an interesting project.

References

[1] I.E. Agency, Global Energy Review: CO_2 Emissions in 2021 Global emissions rebound sharply to highest ever level, International Energy Agency, 2021.
[2] E.a.C.C. Canada, Canadian Environmental Sustainability Indicators: Greenhouse gas emissions, 2023.
[3] K.M.K. Yu, I. Curcic, J. Gabriel, S.C.E. Tsang, Recent advances in CO_2 capture and utilization, ChemSusChem, 1 (2008) 893-899.
[4] M. Aresta, A. Dibenedetto, Utilisation of CO_2 as a chemical feedstock: opportunities and challenges, Dalton Transactions, (2007) 2975-2992.
[5] D.S. Simakov, Renewable synthetic fuels and chemicals from carbon dioxide: fundamentals, catalysis, design considerations and technological challenges, Springer2017.
[6] H.J. Chae, J.-H. Kim, S.C. Lee, H.-S. Kim, S.B. Jo, J.-H. Ryu, T.Y. Kim, C.H. Lee, S.J. Kim, S.-H. Kang, Catalytic technologies for CO hydrogenation for the production of light hydrocarbons and middle distillates, Catalysts, 10 (2020) 99.
[7] Y.A. Daza, J.N. Kuhn, CO_2 conversion by reverse water gas shift catalysis: comparison of catalysts, mechanisms and their consequences for CO_2 conversion to liquid fuels, RSC advances, 6 (2016) 49675-49691.
[8] B. Lu, K. Kawamoto, Preparation of mesoporous CeO_2 and monodispersed NiO particles in CeO_2, and enhanced selectivity of NiO/CeO_2 for reverse water gas shift reaction, Materials Research Bulletin, 53 (2014) 70-78.
[9] Z. Zhao, M. Wang, P. Ma, Y. Zheng, J. Chen, H. Li, X. Zhang, K. Zheng, Q. Kuang, Z.-X. Xie, Atomically dispersed Pt/CeO_2 catalyst with superior CO selectivity in reverse water gas shift reaction, Applied Catalysis B: Environmental, 291 (2021) 120101.
[10] M. Tawalbeh, R.M.N. Javed, A. Al-Othman, F. Almomani, S. Ajith, Unlocking the potential of CO_2 hydrogenation into valuable products using noble metal catalysts: A comprehensive review, Environmental Technology & Innovation, (2023) 103217.
[11] F. Wang, S. He, H. Chen, B. Wang, L. Zheng, M. Wei, D.G. Evans, X. Duan, Active site dependent reaction mechanism over Ru/CeO_2 catalyst toward CO_2 methanation, Journal of the American Chemical Society, 138 (2016) 6298-6305.
[12] S.S. Kim, H.H. Lee, S.C. Hong, The effect of the morphological characteristics of TiO_2 supports on the reverse water–gas shift reaction over Pt/TiO_2 catalysts, Applied Catalysis B: Environmental, 119 (2012) 100-108.
[13] A. Aitbekova, L. Wu, C.J. Wrasman, A. Boubnov, A.S. Hoffman, E.D. Goodman, S.R. Bare, M. Cargnello, Low-temperature restructuring of CeO_2-supported Ru nanoparticles determines selectivity in CO_2 catalytic reduction, Journal of the American Chemical Society, 140 (2018) 13736-13745.
[14] R. Tang, Z. Zhu, C. Li, M. Xiao, Z. Wu, D. Zhang, C. Zhang, Y. Xiao, M. Chu, A. Genest, Ru-catalyzed reverse water gas shift reaction with near-unity selectivity and superior stability, ACS Materials Letters, 3 (2021) 1652-1659.
[15] L. Yang, L. Pastor-Pérez, S. Gu, A. Sepúlveda-Escribano, T. Reina, Highly efficient Ni/CeO_2-Al_2O_3 catalysts for CO_2 upgrading via reverse water-gas shift: Effect of selected transition metal promoters, Applied Catalysis B: Environmental, 232 (2018) 464-471.
[16] L. Yang, L. Pastor-Perez, J.J. Villora-Pico, A. Sepulveda-Escribano, F. Tian, M. Zhu, Y.-F. Han, T. Ramirez Reina, Highly Active and Selective Multicomponent Fe–Cu/CeO_2–Al_2O_3 Catalysts for CO_2 Upgrading via RWGS: Impact of Fe/Cu Ratio, ACS Sustainable Chemistry & Engineering, 9 (2021) 12155-12166.

[17] A.G. Kharaji, A. Shariati, M.A. Takassi, A novel γ-alumina supported Fe-Mo bimetallic catalyst for reverse water gas shift reaction, Chinese Journal of Chemical Engineering, 21 (2013) 1007-1014.
[18] Y. Gao, K. Xiong, B. Zhu, Design of Cu/MoOx for CO_2 Reduction via Reverse Water Gas Shift Reaction, Catalysts, 13 (2023) 684.
[19] B. Bulfin, A. Lowe, K. Keogh, B. Murphy, O. Lubben, S. Krasnikov, I. Shvets, Analytical model of CeO_2 oxidation and reduction, The Journal of Physical Chemistry C, 117 (2013) 24129-24137.
[20] L. Chen, P. Fleming, V. Morris, J.D. Holmes, M.A. Morris, Size-related lattice parameter changes and surface defects in ceria nanocrystals, The Journal of Physical Chemistry C, 114 (2010) 12909-12919.
[21] B. Dai, S. Cao, H. Xie, G. Zhou, S. Chen, Reduction of CO_2 to CO via reverse water-gas shift reaction over CeO_2 catalyst, Korean Journal of Chemical Engineering, 35 (2018) 421-427.
[22] Y. Liu, Z. Li, H. Xu, Y. Han, Reverse water–gas shift reaction over ceria nanocube synthesized by hydrothermal method, Catalysis Communications, 76 (2016) 1-6.
[23] M.W. Iqbal, Y. Yu, D.S.A. Simakov, Enhancing the surface area stability of the cerium oxide reverse water gas shift nanocatalyst via reverse microemulsion synthesis, Catalysis Today, 407 (2023) 230-243.
[24] G. Zhou, B. Dai, H. Xie, G. Zhang, K. Xiong, X. Zheng, CeCu composite catalyst for CO synthesis by reverse water–gas shift reaction: Effect of Ce/Cu mole ratio, Journal of CO_2 Utilization, 21 (2017) 292-301.
[25] T. Zhang, R. Qu, W. Su, J. Li, A novel Ce–Ta mixed oxide catalyst for the selective catalytic reduction of NO_x with NH_3, Applied Catalysis B: Environmental, 176 (2015) 338-346.
[26] C. Sun, P. Beaunier, V. La Parola, L.F. Liotta, P. Da Costa, Ni/CeO_2 nanoparticles promoted by yttrium doping as catalysts for CO_2 methanation, ACS Applied Nano Materials, 3 (2020) 12355-12368.
[27] I. Luisetto, S. Tuti, C. Romano, M. Boaro, E. Di Bartolomeo, J.K. Kesavan, S.S. Kumar, K. Selvakumar, Dry reforming of methane over Ni supported on doped CeO_2: New insight on the role of dopants for CO_2 activation, Journal of CO_2 Utilization, 30 (2019) 63-78.
[28] B. Dai, G. Zhou, S. Ge, H. Xie, Z. Jiao, G. Zhang, K. Xiong, CO_2 reverse water-gas shift reaction on mesoporous M-CeO_2 catalysts, The Canadian Journal of Chemical Engineering, 95 (2017) 634-642.
[29] A.M. Bahmanpour, F. Héroguel, M. Kılıç, C.J. Baranowski, L. Artiglia, U. Röthlisberger, J.S. Luterbacher, O. Kröcher, Cu–Al spinel as a highly active and stable catalyst for the reverse water gas shift reaction, ACS Catalysis, 9 (2019) 6243-6251.
[30] G. Zhou, H. Lan, T. Gao, H. Xie, Influence of Ce/Cu ratio on the performance of ordered mesoporous CeCu composite oxide catalysts, Chemical Engineering Journal, 246 (2014) 53-63.
[31] H.-X. Liu, S.-Q. Li, W.-W. Wang, W.-Z. Yu, W.-J. Zhang, C. Ma, C.-J. Jia, Partially sintered copper–ceria as excellent catalyst for the high-temperature reverse water gas shift reaction, Nature Communications, 13 (2022) 1-11.
[32] P. Ebrahimi, A. Kumar, M. Khraisheh, Combustion synthesis of copper ceria solid solution for CO_2 conversion to CO via reverse water gas shift reaction, International Journal of Hydrogen Energy, 47 (2022) 41259-41267.
[33] S. Eriksson, U. Nylén, S. Rojas, M. Boutonnet, Preparation of catalysts from microemulsions and their applications in heterogeneous catalysis, Applied Catalysis A: General, 265 (2004) 207-219.
[34] M.A. Malik, M.Y. Wani, M.A. Hashim, Microemulsion method: A novel route to synthesize organic and inorganic nanomaterials: 1st Nano Update, Arabian journal of Chemistry, 5 (2012) 397-417.

[35] B.K. Paul, S.P. Moulik, Microemulsions: an overview, Journal of Dispersion Science and Technology 18 (1997) 301-367.
[36] A.M. Pollard, Analytical chemistry in archaeology, Cambridge University Press2007.
[37] S.R. Khan, B. Sharma, P.A. Chawla, R. Bhatia, Inductively coupled plasma optical emission spectrometry (ICP-OES): a powerful analytical technique for elemental analysis, Food Analytical Methods volume, (2022) 1-23.
[38] F.A. Stevie, C.L. Donley, Introduction to x-ray photoelectron spectroscopy, Journal of Vacuum Science & Technology A, 38 (2020).
[39] P. Sinha, A. Datar, C. Jeong, X. Deng, Y.G. Chung, L.-C. Lin, Surface area determination of porous materials using the Brunauer–Emmett–Teller (BET) method: limitations and improvements, The Journal of Physical Chemistry C, 123 (2019) 20195-20209.
[40] D. Dollimore, P. Spooner, A. Turner, The BET method of analysis of gas adsorption data and its relevance to the calculation of surface areas, Surface Technology, 4 (1976) 121-160.
[41] S. Mehanny, H. Ibrahim, L. Darwish, M. Farag, A.-H.M. El-Habbak, E. El-Kashif, Effect of environmental conditions on date palm fiber composites, Date Palm Fiber Composites: Processing, Properties

Applications, (2020) 287-320.
[42] S.L. Schroeder, M. Gottfried, Temperature-programmed desorption (TPD) thermal desorption spectroscopy (TDS), Adv. Phys. Chem. Lab, FU Berlin, (2002) 1-22.
[43] Y. Zhuang, R. Currie, K.B. McAuley, D.S. Simakov, Highly-selective CO_2 conversion via reverse water gas shift reaction over the 0.5 wt% Ru-promoted Cu/ZnO/Al_2O_3 catalyst, Applied Catalysis A: General, 575 (2019) 74-86.
[44] A.R. Symington, R.M. Harker, M.T. Storr, M. Molinari, S.C. Parker, Thermodynamic evolution of cerium oxide nanoparticle morphology using carbon dioxide, J The Journal of Physical Chemistry C, 124 (2020) 23210-23220.
[45] S. Damyanova, C.A. Perez, M. Schmal, J.M.C. Bueno, Characterization of ceria-coated alumina carrier, Applied Catalysis A: General, 234 (2002) 271-282.
[46] P. Panagiotopoulou, D.I. Kondarides, Effect of morphological characteristics of TiO_2-supported noble metal catalysts on their activity for the water–gas shift reaction, Journal of catalysis, 225 (2004) 327-336.
[47] R.-t. Guo, Y. Zhou, W.-g. Pan, J.-n. Hong, W.-l. Zhen, Q. Jin, C.-g. Ding, S.-y. Guo, Effect of preparation methods on the performance of CeO_2/Al_2O_3 catalysts for selective catalytic reduction of NO with NH_3, Journal of Industrial and Engineering Chemistry, 19 (2013) 2022-2025.
[48] A. Martinez-Arias, M. Fernandez-Garcia, L. Salamanca, R. Valenzuela, J. Conesa, J. Soria, Structural and redox properties of ceria in alumina-supported ceria catalyst supports, The Journal of Physical Chemistry B, 104 (2000) 4038-4046.
[49] M. Mogensen, Physical, chemical and electrochemical properties of pure and doped ceria, Solid State Ionics, 129 (2000) 63-94.
[50] K. Mužina, S. Kurajica, G. Dražić, P. Guggenberger, G. Matijašić, True doping levels in hydrothermally derived copper-doped ceria, Journal of Nanoparticle Research, 23 (2021) 1-14.
[51] R. Si, J. Raitano, N. Yi, L. Zhang, S.-W. Chan, M. Flytzani-Stephanopoulos, Structure sensitivity of the low-temperature water-gas shift reaction on Cu–CeO_2 catalysts, Catalysis Today, 180 (2012) 68-80.
[52] Jolm F. Moulder, William F. Stickle, Peter E.'Sobol, K.D. Bomben, Handbook of X-ray Photoelectron Spectroscopy, Perkin-Elmer Corporation, United States of America, 1992.
[53] N.-Y. Kim, G. Kim, H. Sun, U. Hwang, J. Kim, D. Kwak, I.-K. Park, T. Kim, J. Suhr, J.-D. Nam, A nanoclustered ceria abrasives with low crystallinity and high Ce^{3+}/Ce^{4+} ratio for scratch reduction

and high oxide removal rates in the chemical mechanical planarization, Journal of Materials Science, 57 (2022) 12318-12328.
[54] J. Han, J. Meeprasert, P. Maitarad, S. Nammuangruk, L. Shi, D. Zhang, Investigation of the facet-dependent catalytic performance of Fe_2O_3/CeO_2 for the selective catalytic reduction of NO with NH_3, The Journal of Physical Chemistry C, 120 (2016) 1523-1533.
[55] Y. Wang, Z. Chen, P. Han, Y. Du, Z. Gu, X. Xu, G. Zheng, Single-atomic Cu with multiple oxygen vacancies on ceria for electrocatalytic CO_2 reduction to CH_4, ACS Catalysis, 8 (2018) 7113-7119.
[56] W. Shan, Z. Feng, Z. Li, J. Zhang, W. Shen, C. Li, Oxidative steam reforming of methanol on $Ce_{0.9}Cu_{0.1}O_Y$ catalysts prepared by deposition–precipitation, coprecipitation, and complexation–combustion methods, Journal of Catalysis, 228 (2004) 206-217.
[57] A. Guerrero-Ruiz, I. Rodriguez-Ramos, J. Fierro, Dehydrogenation of methanol to methyl formate over supported copper catalysts, Applied Catalysis, 72 (1991) 119-137.
[58] K.N. Rao, P. Venkataswamy, B.M. Reddy, Structural characterization and catalytic evaluation of supported copper–ceria catalysts for soot oxidation, Industrial & Engineering Chemistry Research, 50 (2011) 11960-11969.
[59] C. Hu, Q. Zhu, Z. Jiang, L. Chen, R. Wu, Catalytic combustion of dilute acetone over Cu-doped ceria catalysts, Chemical Engineering Journal, 152 (2009) 583-590.
[60] S. Ewald, O. Hinrichsen, On the interaction of CO_2 with Ni-Al catalysts, Applied Catalysis A: General, 580 (2019) 71-80.
[61] S. Zeng, Y. Wang, S. Ding, J.J. Sattler, E. Borodina, L. Zhang, B.M. Weckhuysen, H. Su, Active sites over CuO/CeO_2 and inverse CeO_2/CuO catalysts for preferential CO oxidation, Journal of Power Sources, 256 (2014) 301-311.